STATE RESEARCH CENTER OF RUSSIA

INSTITUTE FOR HIGH ENERGY PHYSICS

IHEP 99-63

V.Bumazhnov, V.Kochetkov[1], V.Semenov, A.Soldatov

LHC-B CALORIMETER TRIGGER EFFICIENCY FOR PROCESS $pp \to (B_d^0 \to \pi^+\pi^-) + X$ AT $\sqrt{S}$ =14 TeV

[1]ITEP, Moscow

Protvino 1999

UDK 539.1.074 M–24

Abstract

Bumazhnov V. et al. LHC-B calorimeter trigger efficiency for process $pp \to (B_d^0 \to \pi^+\pi^-) + X$ at $\sqrt{S}$ =14 TeV: IHEP Preprint 99-63. – Protvino, 1999. – p. 50, figs. 28, tables 13, refs.: 4.

The influence of LHCB hadronic calorimeter nuclear length on the trigger efficiency ϵ for $pp \to (B_d^0 \to \pi^+\pi^-) + X$ has been investigated. The dependences of ϵ on the transverse energy E_t of two most energetic event particles have been obtained. The influence of electronics noise and precluster isolation parameter on ϵ has been investigated. Registration efficiency of minimum bias and pile-up events as B_d^0-event candidates has been investigated too.

Аннотация

Бумажнов В. и др. Эффективность калориметрического триггера в эксперименте LHC-B для процесса $pp \to (B_d^0 \to \pi^+\pi^-) + X$ at $\sqrt{S}$ =14 TeV: Препринт ИФВЭ 99-63. – Протвино, 1999. – 50 с., 28 рис., 13 табл., библиогр.: 4.

В работе исследовано влияние ядерной длины адронного калориметра экспериментальной установки LHC-B на эффективность триггера ϵ для процесса $pp \to (B_d^0 \to \pi^+\pi^-) + X$. Получены зависимости эффективности ϵ от значений поперечной энергии E_t двух самых быстрых частиц события. Исследовано влияние шумов электроники и параметра изолированности прекластера, образованного в preshower, на эффективность регистрации B_d^0-события. Получены также эффективности регистрации фона от minimum bias и pile-up событий в качестве кандидатов на B_d^0-события.

Introduction

The unitary Cabibbo-Kobayashi-Moskawa quark mixing matrix can be represented by means of Wolfenstein[1] parameterization as

$$V = \begin{pmatrix} V_{ud} & V_{us} & V_{ub} \\ V_{cd} & V_{cs} & V_{cb} \\ V_{td} & V_{ts} & V_{tb} \end{pmatrix} = \begin{pmatrix} 1-\frac{1}{2}\lambda^2 & \lambda & A\lambda^3(\rho - i\eta) \\ -\lambda & 1-\frac{1}{2}\lambda^2 & A\lambda^2 \\ A\lambda^3(1-\rho-i\eta) & -A\lambda^2 & 1 \end{pmatrix}. \quad (1)$$

To determine ρ and η parameters, different modes of B^0-decays will be investigated by LHC-B experiment. One of these decays is the $B_d^0 \to \pi^+\pi^-$.

As the cross section ratio of the $pp \to (B_d^0 \to \pi^+\pi^-) + X$ and $pp \to$ (minimum bias) events is about 10^{-7}, we must select the $pp \to (B_d^0 \to \pi^+\pi^-) + X$ process properly.

1. Description of calorimeter structure

To calculate trigger efficiency ϵ for process $pp \to (B_d^0 \to \pi^+\pi^-) + X$ at $\sqrt{S} = 14$ TeV the GEANT3.21 code has been used. Using this code the combined calorimeter of 8×8 m^2 size consisting of electromagnetic and united to it by means of 5 cm iron plate hadronic calorimeter has been simulated.

The illustration of the combined calorimeter module is shown in fig 1.

The lead-scintillator electromagnetic calorimeter consists of individual modules of 4×4 cm^2 cross-section sizes, each of them represents the set of $70(25X_0)$ successive layers of 2 mm lead plate and 4 mm polystyrene scintillator plate (tile).

It should be noted that the results of this work will remain valid in case of using $21X_0$ lead-scintillator electromagnetic calorimeter.

The first 9 layers in the beginning of electromagnetic calorimeter are used simultaneously as a preshower.

The iron-scintillator hadronic calorimeter consists of individual modules of 4×4 cm^2 cross-section sizes too. Each module represents the set of successive layers of 2.4 cm iron plate and 0.6 cm polystyrene scintillator plate. The number of module layers was varied and chosen to be $51(7.2\lambda_{nucl})$, $25(3.5\lambda_{nucl})$ and $14(2\lambda_{nucl})$, respectively.

There is a square hole with sizes of 64×64 cm^2 in the center of the combined calorimeter.

2. Details of calculations

The calculations have been made for GEANT energy threshold values of 0.2 MeV and 10 MeV for e, γ and hadrons, muons, respectively.

The light collection from the preshower, electromagnetic and hadronic calorimeter modules is accomplished independently. The PMT set-up for the preshower and electromagnetic calorimeter is placed before the electromagnetic calorimeter. For the hadronic calorimeter the PMT set-up is placed behind it.

The light collection A_j from any preshower, electromagnetic and hadronic calorimeter module j is determined as

$$A_j \sim \sum_{i=1}^{N_{tile}} E_{i,j} L(x_i) \tag{2}$$

where $E_{i,j}$ is an energy deposited by a particle in the scintillator tile i of the module j. The function $L(x_i)$ describes a light attenuation in a wavelength shifter fiber and can be defined as

$$L(x_i) = exp(-x_i/\lambda_{att}) + exp(-(l_f - x_i)/\lambda_{att}), \tag{3}$$

where l_f is a fiber length, x_i is a distance between a tile center and PMT while λ_{att} is a fiber attenuation length.

The calorimeter calibration has been accomplished by means of 10 Gev/c π^+. If initial π^+ had energy E_0, then electromagnetic C_{EMcal} and hadronic C_{Hcal} calibration constants were determined by minimizing the following expression $(E - E_0)^2$ on these constants, where

$$E = C_{EMcal} \sum_j A_j^{EMcal} + C_{Hcal} \sum_j A_j^{Hcal} \tag{4}$$

A set of calibration constants for different hadronic calorimeter nuclear length λ_{Hcal} and different λ_{att} values was obtained and used in this work for all further calculations.

The π^+-beams with initial momenta 5, 10, 50, 100, 250, 550 GeV/c were simulated and used to determine the energy resolution of the combined calorimeter. The π^+-beams hit electromagnetic calorimeter perpendicular to it 's front surface.

The distributions on reconstruction energy of $\pi^+ - mesons$ having initial momenta 5, 10, 50, 100, 250, 550 GeV/c are shown in figs 2, 3 for $\lambda_{Hcal} = 7.2, 3.5\ \lambda_{nucl}$, respectively.

Significant longitudinal hadron shower fluctuations resulted in the tails for small values of λ_{att} in the case of $\lambda_{Hcal} = 7.2\ \lambda_{nucl}$.

The longitudinal energy leakage was observed when using 3.5 λ_{nucl} hadronic modules. It follows from figs 4, 5 that this energy leakage leads to increasing constant C at fitting calorimeter energy resolution by function $\frac{\sigma_E}{E} = \frac{\sigma}{\sqrt{E}} \oplus C$.

3. Rejection of e,γ

To understand what energy is deposited in the preshower by high energy hadrons and how many preshower cells are lit up, the combined calorimeter cells were hit by 10 GeV/c π^+ over all it's front surface by a uniform law. The point from which π^+-mesons came out was 12 m distance from the front calorimeter surface.

Similar simulation was made for 10 GeV/c γ.

The distributions of energy deposited in the preshower by such π^+ and γ are presented in fig. 6. We can see that these distributions for π^+ and γ are significantly different. This difference allows us to reject the electromagnetic particles (e, γ) of event.

From this figure the cut $E_{cut} = 0.03$ GeV on the energy deposited by high energy hadron in the preshower was chosen. The particles depositing the energy $E > E_{cut}$ in the preshower should be rejected.

The distributions on the number of preshower cells lit by 10 GeV/c π^+ and γ are shown in fig. 7. They are significantly different too.

From this figure the cut $N_{cut} = 4$ on the number of lit preshower cells was chosen. The particles that caused the number of lit preshower cells $N > N_{cut}$ should be rejected.

The additional (e, γ)-rejection can be obtained by means of a cut on the ratio $\beta = \frac{E_{EMcal}}{E_{Hcal}}$ of the energy deposited in the electromagnetic calorimeter to the hadronic one. The distributions of $\frac{E_{EMcal}}{E_{Hcal}}$ for 10 GeV/c π^+ and γ are shown in figs. 8, 9 for the hadronic calorimeter nuclear length $\lambda_{Hcal} = 3.5\ \lambda_{nucl}$ and the fiber attenuation length $\lambda_{att} = 150$ cm.

From these figures the cut $\beta_{cut} = 60$ was chosen. The particles for which $\beta > \beta_{cut}$ must be rejected.

4. Event simulation

The 500 events of process $pp \to (B_d^0 \to \pi^+\pi^-) + X$ at $\sqrt{S}$ =14 TeV have been simulated by means of PYTHIA5.7 [4]. The channel $B_d^0 \to \pi^+\pi^-$ was added to the table of particle data. All the channels except $B_d^0 \to \pi^+\pi^-$ were closed for B_d^0-meson and opened for $\bar{B}_d^0$. All the unstable particles were allowed to decay in the range of $0 \leq Z \leq 12m$ between the interaction vertex and the preshower.

It should be noted that in each event both π-mesons from B_d^0-decay hit the front surface of the electromagnetic calorimeter.

The 3000 minimum bias events including single and double diffraction events as well as elastic and low P_t events were simulated.

The 1200 pile-up events consisting of n minimum bias events were simulated too. Here n was distributed by Poisson with $< n >= 2$.

The particles of each event were traced by GEANT3.21 code through the calorimeter matter. It should be noted that the matter between the vertex of interaction and the combined calorimeter as well as a magnetic field were not taken into account in this work. The vertex of interaction was 12 meters apart from the front surface of electromagnetic calorimeter.

The energy deposition in the cells of the preshower, electromagnetic and hadronic parts of the combined calorimeter was determined by all the event particles hitting the calorimeter.

5. Precluster finding

The di-hadron algorithm suggested in LOI [2] to select $B_d^0 \to \pi^+\pi^-$ events has been used in this work.

We determine a precluster as a set of lit preshower cells having one common point of contact at least. Let us define the distance R between two preclusters as a minimum distance R_{ij} between the centers of two cells belonging to different preclusters

$$R \quad = \quad \min_{i,j} \quad R_{i,j} \tag{5}$$

where i, j runs over the cells of the first and second precluster, respectively.

As a measurement unit of R, we took the lateral size (width or height) of the calorimeter cell. For each precluster of an event the minimum distance R_{isol} between this precluster and all other preclusters was determined.

Using the data of energy deposition in the preshower cells, the precluster finding was carried out and their parameters (R_{isol}, energy deposition $E_{preclust}$ and the number of lit cells $N_{preclust}$ in the preshower) were determined. From this moment any precluster was considered as a particle.

The cuts on energy deposition $E_{preclust} \leq E_{cut}$, the number of lit cells $N_{preclust} \leq N_{cut}$ and $R_{isol} \geq R_{cut}$ were applied to the precluster parameters. We demanded that there would be no preclusters in the distance of 6 preshower cells from the precluster under consideration. So, we set $R_{cut} = 6$. The preclusters that passed these cuts are considered as hadrons.

It should be noted that these cuts will also reject the groups of particles which are close to each other in space (pile-up particles).

6. Cluster finding

Now we can look for the clusters of 3×3 cells in the electromagnetic and hadronic calorimeters with respect to those precluster cells which have been already found. It should be noted that one cluster cell can consist of some calorimeter modules which determine the cluster cell sizes. The cluster cell sizes in electromagnetic and hadronic calorimeters may be different.

Knowing the addresses of precluster cells, the 8×8 cm^2 hadronic calorimeter cluster cell with maximum energy deposition was searched for. The cluster boundaries in hadronic calorimeter were determined with respect to this found cell. In the electromagnetic calorimeter the cell with maximum energy deposition was not searched for and the cluster boundaries were determined by precluster information only.

It should be noted that cluster sizes in hadronic and electromagnetic calorimeters were 3×3 cells. But the lateral sizes of hadronic and electromagnetic calorimeter cluster cells were 8×8 cm^2 and 4×4 cm^2, respectively.

The cluster energy in the electromagnetic calorimeter E_{clust}^{EMcal} and in hadronic one E_{clust}^{Hcal} has been determined for all clusters of an event which passed through the cuts. The addition cut $\frac{E_{clust}^{EMcal}}{E_{clust}^{Hcal}} < \beta_{cut}$ has been applied to reject e,γ which passed through the previous cuts.

The total cluster energy E_{clust} was determined as

$$E_{clust} = E_{clust}^{EMcal} + E_{clust}^{Hcal} \quad . \tag{6}$$

Then, the transverse cluster energy E_t was determined according to

$$E_t = E_{clust} \sin\theta \tag{7}$$

where θ is the angle between beam axes and the vector directed from the vertex of interaction to a precluster.

This procedure has been performed for all clusters of an event. Then the event clusters were ordered on transverse energy. Two clusters having the maximum and next value of transverse energy were kept for the following analysis. Hereafter, we shall identify these two clusters as π-mesons with transverse energy meeting the following expression $E_t^{\pi_1} > E_t^{\pi_2}$.

7. Distributions on trigger variables

The distribution on $E_t^{\pi_1}$ for different fiber attenuation length values λ_{att} and different values of hadronic calorimeter nuclear length for B_d^0, minimum bias and pile-up events are shown in figs. 10, 11, 12.

It follows from these figures that $E_t^{\pi_1}$ for B_d^0-events ($< E_t^{\pi_1} \sim 1.7$ GeV$>$), is considerably harder than for minimum bias and pile-up events ($< E_t^{\pi_1} \sim 0.7$ GeV$>$).

The similar distributions on $E_t^{\pi_2}$ are represented in figs. 13, 14, 15. The same conclusions may be drawn. Moreover, it follows from these figures that nuclear length of hadronic calorimeter influences the $E_t^{\pi_1}$ and $E_t^{\pi_2}$ distributions weakly.

The distribution on the energy $E_{visible}$ deposited in the combined calorimeter for B_d^0, minimum bias and pile-up events for different fiber attenuation length values λ_{att} and different values of hadronic calorimeter nuclear length are shown in figs. 16, 17, 18. These distributions are significantly different in the range of $E_{visible} < 130$ GeV. This point could be used to reject the minimum bias background. The events which fulfill the following requirement $E_{visible} < 130$ GeV could be rejected. Moreover, it should be noted that the nuclear length of hadronic calorimeter influences the $E_{visible}$-distribution weakly.

The distribution on effective mass $M_{\pi_1\pi_2}$ of two selected π-mesons for B_d^0, minimum bias and pile-up events in the case of different values of hadronic calorimeter nuclear length and when $E_t^{\pi_1} > 0.5$ GeV, $E_t^{\pi_2} > 0.3$ GeV, $\lambda_{att} = 150$ cm are shown in figs. 19, 20, 21. It follows from these figures that nuclear length of hadronic calorimeter influences the $M_{\pi_1\pi_2}$-distribution weakly.

The effective mass cut $M_{cut} = 0.5$ GeV has been chosen from these figures. The events which met the following requirement $M_{\pi_1\pi_2} < 0.5$ GeV were rejected.

It should be noted that this cut is low significant and may be omitted.

8. Trigger efficiency

The trigger efficiency ϵ was defined as a ratio of the number of events N_{pass} passing all the implied cuts to the total number of processed events N_{tot}

$$\epsilon = \frac{N_{pass}}{N_{tot}} \quad . \tag{8}$$

The dependence of trigger efficiency ϵ on the first pion transverse energy $E_t^{\pi_1}$ for the process $pp \to (B_d^0 \to \pi^+\pi^-) + X$, when the second transverse energy cut $E_t^{\pi_2} > 0.5$ GeV is applied, is shown in fig. 22 and tables $1-3$ for $\lambda_{att} = 150$ cm.

To see the effect of cut on each trigger variable, we showed in the tables the efficiency after each cut. It should be noted that $E_{visible}$ and effective mass $M_{\pi_1\pi_2}$ cuts influence the efficiency weakly.

It follows from this figure and tables that ϵ decreases with $E_t^{\pi_1}$ increase.

The dependence of efficiency ϵ to register a minimum bias or pile-up event as a B_d^0-event candidate on $E_t^{\pi_1}$ is shown in the same figure and tables $4-9$ for the same cuts. It is seen that this efficiency is significantly less than one for B_d^0-events.

The rate of decreasing efficiency ϵ with $E_t^{\pi_1}$ increasing for minimum bias and pile-up events is considerably larger than that for B_d^0-events.

The dependence of efficiency for B_d^0-events on the minimum bias and pile-up one in the case of $E_t^{\pi_2} > 0.3$ and 0.5 GeV , λ_{att} =150 cm and $\lambda_{Hcal} = 2,\ 3.5,\ 7.2\ \lambda_{nucl}$ is shown in fig. 23. It

follows from these data that ϵ depends on the nuclear length of hadronic calorimeter λ_{Hcal} weakly in the range of $3.5\lambda_{nucl} \leq \lambda_{Hcal} \leq 7.2\lambda_{nucl}$. The results get worse slightly for $\lambda_{Hcal} = 2\lambda_{nucl}$.

The dependence of ϵ for B_d^0 -events on λ_{att} is shown in tables 10, 1, 11 in the case of $E_t^{\pi_2} > 0.5$ GeV and λ_{att} =70, 150 and 10000 cm, respectively.

It follows from these data that ϵ increases with increasing λ_{att}.

8.1. Dependence of efficiency on the R_{isol}

The dependence of efficiency for B_d^0-events on the minimum bias and pile-up one in the case of $R_{isol} = 3$ and 1 is shown in figs 24, 25, respectively. It follows from these figures that the smaller R_{isol} the larger efficiency for B_d^0 as well as for minimum bias and pile-up events. It happens because R_{isol} decrease leads to increasing the number of selected preclusters. But in this case the number of selected preclusters with shower overlapping in the calorimeter increases too.

The dependence of efficiency for B_d^0-events on the minimum bias and pile-up one when we demand that any precluster should have only one lit cell ($N_{cut} = 1$) is shown in fig. 26. We can see that ϵ decreases for both B_d^0 and minimum bias and pile-up events. It happens because the hadrons hit preshower near the cell boundaries light up more than one preshower cell and therefore are rejected.

8.2. Dependence of efficiency on the cluster cell sizes

The dependence of efficiency for B_d^0 and minimum bias events on the cluster cell sizes is represented for $\lambda_{Hcal} = 3.5\lambda_{nucl}$, $\lambda_{att} = 150$ cm and $E_t^{\pi_2} > 0.5$ GeV in tables 13, 14, respectively.

Here ϵ_1 corresponds to the case when the cluster cell sizes in electromagnetic and hadronic calorimeters have been chosen as 4×4 cm^2 and 8×8 cm^2, respectively. The maximum energy deposition cluster cell was searched for electromagnetic and hadronic calorimeter clusters.

ϵ_2 corresponds to the case when the cluster cell sizes in electromagnetic and hadronic calorimeters have been chosen as 4×4 cm^2 and 8×8 cm^2, respectively. The maximum energy deposition cluster cell was searched for hadronic calorimeter clusters and was not searched for electromagnetic ones.

ϵ_3 corresponds to the case when the cluster cell sizes in electromagnetic and hadronic calorimeters have been chosen as 4×4 cm^2 and 8×8 cm^2, respectively. The maximum energy deposition cluster cell was not searched for electromagnetic and hadronic calorimeter clusters.

ϵ_4 corresponds to the case when the cluster cell sizes in electromagnetic and hadronic calorimeters have been chosen as 8×8 cm^2, respectively. The maximum energy deposition cluster cell was searched for electromagnetic and hadronic calorimeter clusters.

ϵ_5 corresponds to the case when the cluster cell sizes in electromagnetic and hadronic calorimeters have been chosen as 4×4 cm^2, respectively. The maximum energy deposition cluster cell was not searched for electromagnetic and hadronic calorimeter clusters.

It follows from these data that the larger cluster cell sizes the larger efficiency for both B_d^0 and minimum bias events.

8.3. Dependence of efficiency on the electronic noise

To understand how the electronic noise will influence the efficiency for B_d^0, minimum bias and pile-up events, we supposed that electronic noise in a preshower cell has the Gaussian distribution with $\sigma_{noise} = 0.5$ MeV.

In this connection an energy cut to an amplitude value A_j measured in the preshower cell j has been applied: $A_j \geq A_{cut}^{noise}$.

The dependence of efficiency for B_d^0-events on the minimum bias and pile-up one in the case of $A_{cut}^{noise} = 1$ and 2 MeV is shown in fig. 27, 28 respectively. We can see that for $A_{cut}^{noise} = 1$ MeV ϵ is significantly smaller with respect to the case of electronic noise lack.

It happens because the preclusters created by electronic noise in the distance of $R \leq R_{isol}$ from any true precluster will reject this true precluster. In the case of $A_{cut}^{noise} = 2$ MeV the electronic noise preclusters are rejected by large A_{cut}^{noise} value.

Moreover, some part of true preclusters which was rejected in the case of electronic noise lack now can pass the cut $N \leq N_{cut}$ and it leads to the increase of ϵ. We can see it in fig. 28.

The choice of A_{cut}^{noise} must be made carefully because for too large A_{cut}^{noise} an additional part of the pile-up background can pass all the cuts.

9. Conclusions

1. The trigger efficiency ϵ for $pp \to (B_d^0 \to \pi^+\pi^-) + X$ $\sqrt{S} = 14$ TeV depends weakly on the nuclear length of hadronic calorimeter in the range of $3.5\lambda_{nucl} \leq \lambda_{Hcal} \leq 7.2\lambda_{nucl}$.
2. The rate of decreasing efficiency ϵ for B_d^0-events at increasing $E_t^{\pi_1}$ is considerably smaller than the one for minimum bias and pile-up events.
3. For the given cluster sizes of 3×3 cells, the trigger efficiency ϵ depends significantly on whether the maximum energy deposition cell is searched for in electromagnetic and hadronic calorimeters or not.
4. The trigger efficiency ϵ depends significantly on the precluster isolation parameter.
5. The trigger efficiency ϵ depends significantly on the choice of A_{cut}^{noise} value.

Table 1. The trigger efficiency ϵ for $B_d^0 \to \pi^+\pi^-$ events at hadronic calorimeter nuclear length of 7.2 λ_{nucl} and fiber attenuation length of $\lambda_{att} = 150$ cm. The cluster cell sizes in electromagnetic and hadronic calorimeters have been chosen as 4×4 cm^2 and 8×8 cm^2, respectively. The maximum energy deposition cluster cell was searched for hadronic calorimeter clusters and was not searched for electromagnetic ones. The following cuts $E_{preclust} \leq 0.03$ GeV, $N_{preclust} \leq 4$, $R_{isol} \geq 6$ and $\frac{E_{clust}^{EMcal}}{E_{clust}^{Hcal}} \leq 60$ have been applied during precluster and cluster finding.

$E_t^{\pi_1}(GeV) >$	1.0	1.5	2.0	2.5	3.0
$\epsilon\%$	52.80	40.00	30.20	23.20	18.20
	3.25	2.83	2.46	2.15	1.91
$E_t^{\pi_2} > 0.50GeV$					
$\epsilon\%$	35.80	27.60	21.60	15.60	12.20
	2.68	2.35	2.08	1.77	1.56
$M_{\pi_1\pi_2} > 0.5GeV$					
$\epsilon\%$	34.80	26.80	21.40	15.60	12.20
	2.64	2.32	2.07	1.77	1.56
$E_{visible} > 130.0GeV$					
$\epsilon\%$	34.20	26.40	21.20	15.60	12.20
	2.62	2.30	2.06	1.77	1.56

Table 2. The trigger efficiency ϵ for $B_d^0 \to \pi^+\pi^-$ events at hadronic calorimeter nuclear length of 3.5 λ_{nucl} and fiber attenuation length of $\lambda_{att} = 150$ cm. The cluster cell sizes in electromagnetic and hadronic calorimeters have been chosen as 4×4 cm^2 and 8×8 cm^2, respectively. The maximum energy deposition cluster cell was searched for hadronic calorimeter clusters and was not searched for electromagnetic ones. The following cuts $E_{preclust} \leq 0.03$ GeV, $N_{preclust} \leq 4$, $R_{isol} \geq 6$ and $\frac{E_{clust}^{EMcal}}{E_{clust}^{Hcal}} \leq 60$ have been applied during precluster and cluster finding.

$E_t^{\pi_1}(GeV) >$	1.0	1.5	2.0	2.5	3.0
$\epsilon\%$	54.20	40.00	31.40	24.00	18.20
	3.29	2.83	2.51	2.19	1.91
$E_t^{\pi_2} > 0.50GeV$					
$\epsilon\%$	37.40	27.40	20.80	15.80	11.80
	2.73	2.34	2.04	1.78	1.54
$M_{\pi_1\pi_2} > 0.5GeV$					
$\epsilon\%$	36.20	26.60	20.40	15.40	11.60
	2.69	2.31	2.02	1.75	1.52
$E_{visible} > 130.0GeV$					
$\epsilon\%$	35.40	26.20	20.20	15.40	11.60
	2.66	2.29	2.01	1.75	1.52

Table 3. The trigger efficiency ϵ for $B_d^0 \to \pi^+\pi^-$ events at hadronic calorimeter nuclear length of 2.0 λ_{nucl} and fiber attenuation length of $\lambda_{att} = 150$ cm. The cluster cell sizes in electromagnetic and hadronic calorimeters have been chosen as 4×4 cm^2 and 8×8 cm^2, respectively. The maximum energy deposition cluster cell was searched for hadronic calorimeter clusters and was not searched for electromagnetic ones. The following cuts $E_{preclust} \leq 0.03$ GeV, $N_{preclust} \leq 4$, $R_{isol} \geq 6$ and $\frac{E_{clust}^{EMcal}}{E_{clust}^{Hcal}} \leq 60$ have been applied during precluster and cluster finding.

$E_t^{\pi_1}(GeV) >$	1.0	1.5	2.0	2.5	3.0
$\epsilon\%$	56.80	37.40	28.40	20.20	15.80
	3.37	2.73	2.38	2.01	1.78
$E_t^{\pi_2} > 0.50GeV$					
$\epsilon\%$	39.00	25.80	19.00	13.00	9.80
	2.79	2.27	1.95	1.61	1.40
$M_{\pi_1\pi_2} > 0.5GeV$					
$\epsilon\%$	37.80	24.80	18.60	12.80	9.60
	2.75	2.23	1.93	1.60	1.39
$E_{visible} > 130.0GeV$					
$\epsilon\%$	37.00	24.40	18.40	12.80	9.60
	2.72	2.21	1.92	1.60	1.39

Table 4. The efficiency ϵ to register a minimum bias event as a $B_d^0 \to \pi^+\pi^-$ event candidate at hadronic calorimeter nuclear length of 7.2 λ_{nucl} and fiber attenuation length of $\lambda_{att} = 150$ cm. The cluster cell sizes in electromagnetic and hadronic calorimeters have been chosen as 4×4 cm^2 and 8×8 cm^2, respectively. The maximum energy deposition cluster cell was searched for hadronic calorimeter clusters and was not searched for electromagnetic ones. The following cuts $E_{preclust} \leq 0.03$ GeV, $N_{preclust} \leq 4$, $R_{isol} \geq 6$ and $\frac{E_{clust}^{EMcal}}{E_{clust}^{Hcal}} \leq 60$ have been applied during precluster and cluster finding.

$E_t^{\pi_1}(GeV) >$	1.0	1.5	2.0	2.5	3.0
$\epsilon\%$	13.20	4.27	1.73	0.57	0.20
	0.66	0.38	0.24	0.14	0.08
$E_t^{\pi_2} > 0.50GeV$					
$\epsilon\%$	9.40	3.37	1.43	0.53	0.20
	0.56	0.33	0.22	0.13	0.08
$M_{\pi_1\pi_2} > 0.5GeV$					
$\epsilon\%$	8.50	3.07	1.33	0.50	0.20
	0.53	0.32	0.21	0.13	0.08
$E_{visible} > 130.0GeV$					
$\epsilon\%$	7.37	2.90	1.23	0.43	0.20
	0.50	0.31	0.20	0.12	0.08

Table 5. The efficiency ϵ to register a minimum bias event as a $B_d^0 \to \pi^+\pi^-$ event candidate at hadronic calorimeter nuclear length of 3.5 λ_{nucl} and fiber attenuation length of $\lambda_{att} = 150$ cm. The cluster cell sizes in electromagnetic and hadronic calorimeters have been chosen as 4×4 cm^2 and 8×8 cm^2, respectively. The maximum energy deposition cluster cell was searched for hadronic calorimeter clusters and was not searched for electromagnetic ones. The following cuts $E_{preclust} \leq 0.03$ GeV, $N_{preclust} \leq 4$, $R_{isol} \geq 6$ and $\frac{E_{clust}^{EMcal}}{E_{clust}^{Hcal}} \leq 60$ have been applied during precluster and cluster finding.

$E_t^{\pi_1}(GeV) >$	1.0	1.5	2.0	2.5	3.0
$\epsilon\%$	14.50	4.63	1.93	0.53	0.30
	0.70	0.39	0.25	0.13	0.10
$E_t^{\pi_2} > 0.50GeV$					
$\epsilon\%$	10.23	3.63	1.67	0.47	0.23
	0.58	0.35	0.24	0.12	0.09
$M_{\pi_1\pi_2} > 0.5GeV$					
$\epsilon\%$	9.47	3.20	1.50	0.43	0.20
	0.56	0.33	0.22	0.12	0.08
$E_{visible} > 130.0GeV$					
$\epsilon\%$	8.07	2.90	1.40	0.37	0.20
	0.52	0.31	0.22	0.11	0.08

Table 6. The efficiency ϵ to register a minimum bias event as a $B_d^0 \to \pi^+\pi^-$ event candidate at hadronic calorimeter nuclear length of 2.0 λ_{nucl} and fiber attenuation length of $\lambda_{att} = 150$ cm. The cluster cell sizes in electromagnetic and hadronic calorimeters have been chosen as 4×4 cm^2 and 8×8 cm^2, respectively. The maximum energy deposition cluster cell was searched for hadronic calorimeter clusters and was not searched for electromagnetic ones. The following cuts $E_{preclust} \leq 0.03$ GeV, $N_{preclust} \leq 4$, $R_{isol} \geq 6$ and $\frac{E_{clust}^{EMcal}}{E_{clust}^{Hcal}} \leq 60$ have been applied during precluster and cluster finding.

$E_t^{\pi_1}(GeV) >$	1.0	1.5	2.0	2.5	3.0
$\epsilon\%$	15.37	5.23	2.33	1.03	0.50
	0.72	0.42	0.28	0.19	0.13
$E_t^{\pi_2} > 0.50GeV$					
$\epsilon\%$	10.53	3.77	1.83	0.87	0.40
	0.59	0.35	0.25	0.17	0.12
$M_{\pi_1\pi_2} > 0.5GeV$					
$\epsilon\%$	9.53	3.40	1.70	0.73	0.37
	0.56	0.34	0.24	0.16	0.11
$E_{visible} > 130.0GeV$					
$\epsilon\%$	8.13	2.87	1.50	0.57	0.27
	0.52	0.31	0.22	0.14	0.09

Table 7. The efficiency ϵ to register a pile-up event as a $B_d^0 \to \pi^+\pi^-$ event candidate at hadronic calorimeter nuclear length of 7.2 λ_{nucl} and fiber attenuation length of $\lambda_{att} = 150$ cm. The cluster cell sizes in electromagnetic and hadronic calorimeters have been chosen as 4×4 cm^2 and 8×8 cm^2, respectively. The maximum energy deposition cluster cell was searched for hadronic calorimeter clusters and was not searched for electromagnetic ones. The following cuts $E_{preclust} \leq 0.03$ GeV, $N_{preclust} \leq 4$, $R_{isol} \geq 6$ and $\frac{E_{clust}^{EMcal}}{E_{clust}^{Hcal}} \leq 60$ have been applied during precluster and cluster finding.

$E_t^{\pi_1}(GeV) >$	1.0	1.5	2.0	2.5	3.0
$\epsilon\%$	20.92	5.92	2.17	0.83	0.58
	1.32	0.70	0.42	0.26	0.22
$E_t^{\pi_2} > 0.50GeV$					
$\epsilon\%$	15.25	4.67	1.75	0.67	0.58
	1.13	0.62	0.38	0.24	0.22
$M_{\pi_1\pi_2} > 0.5GeV$					
$\epsilon\%$	13.83	4.42	1.75	0.67	0.58
	1.07	0.61	0.38	0.24	0.22
$E_{visible} > 130.0GeV$					
$\epsilon\%$	12.92	4.33	1.75	0.67	0.58
	1.04	0.60	0.38	0.24	0.22

Table 8. The efficiency ϵ to register a pile-up event as a $B_d^0 \to \pi^+\pi^-$ event candidate at hadronic calorimeter nuclear length of 3.5 λ_{nucl} and fiber attenuation length of $\lambda_{att} = 150$ cm. The cluster cell sizes in electromagnetic and hadronic calorimeters have been chosen as 4×4 cm^2 and 8×8 cm^2, respectively. The maximum energy deposition cluster cell was searched for hadronic calorimeter clusters and was not searched for electromagnetic ones. The following cuts $E_{preclust} \leq 0.03$ GeV, $N_{preclust} \leq 4$, $R_{isol} \geq 6$ and $\frac{E_{clust}^{EMcal}}{E_{clust}^{Hcal}} \leq 60$ have been applied during precluster and cluster finding.

$E_t^{\pi_1}(GeV) >$	1.0	1.5	2.0	2.5	3.0
$\epsilon\%$	22.83	7.83	2.50	0.83	0.50
	1.38	0.81	0.46	0.26	0.20
$E_t^{\pi_2} > 0.50GeV$					
$\epsilon\%$	17.75	6.50	2.08	0.75	0.50
	1.22	0.74	0.42	0.25	0.20
$M_{\pi_1\pi_2} > 0.5GeV$					
$\epsilon\%$	16.25	6.17	2.08	0.75	0.50
	1.16	0.72	0.42	0.25	0.20
$E_{visible} > 130.0GeV$					
$\epsilon\%$	15.50	5.67	2.08	0.75	0.50
	1.14	0.69	0.42	0.25	0.20

Table 9. The efficiency ϵ to register a pile-up event as a $B_d^0 \to \pi^+\pi^-$ event candidate at hadronic calorimeter nuclear length of 2.0 λ_{nucl} and fiber attenuation length of $\lambda_{att} = 150$ cm. The cluster cell sizes in electromagnetic and hadronic calorimeters have been chosen as 4×4 cm^2 and 8×8 cm^2, respectively. The maximum energy deposition cluster cell was searched for hadronic calorimeter clusters and was not searched for electromagnetic ones. The following cuts $E_{preclust} \leq 0.03$ GeV, $N_{preclust} \leq 4$, $R_{isol} \geq 6$ and $\frac{E_{clust}^{EMcal}}{E_{clust}^{Hcal}} \leq 60$ have been applied during precluster and cluster finding.

$E_t^{\pi_1}(GeV) >$	1.0	1.5	2.0	2.5	3.0
$\epsilon\%$	24.17	9.17	2.58	1.25	0.33
	1.42	0.87	0.46	0.32	0.17
$E_t^{\pi_2} > 0.50GeV$					
$\epsilon\%$	19.42	7.67	2.17	0.92	0.25
	1.27	0.80	0.42	0.28	0.14
$M_{\pi_1\pi_2} > 0.5GeV$					
$\epsilon\%$	17.83	7.08	2.17	0.92	0.25
	1.22	0.77	0.42	0.28	0.14
$E_{visible} > 130.0GeV$					
$\epsilon\%$	17.00	6.75	2.17	0.92	0.25
	1.19	0.75	0.42	0.28	0.14

Table 10. The trigger efficiency ϵ for $B_d^0 \to \pi^+\pi^-$ events at hadronic calorimeter nuclear length of 7.2 λ_{nucl} and fiber attenuation length of $\lambda_{att} = 70$ cm. The cluster cell sizes in electromagnetic and hadronic calorimeters have been chosen as 4×4 cm^2 and 8×8 cm^2 respectively. The maximum energy deposition cluster cell was searched for hadronic calorimeter clusters and was not searched for electromagnetic ones. The following cuts $E_{preclust} \leq 0.03$ GeV, $N_{preclust} \leq 4$, $R_{isol} \geq 6$ and $\frac{E_{clust}^{EMcal}}{E_{clust}^{Hcal}} \leq 60$ have been applied during precluster and cluster finding.

$E_t^{\pi_1}(GeV) >$	1.0	1.5	2.0	2.5	3.0
$\epsilon\%$	49.60	37.40	27.40	20.60	14.60
	3.15	2.73	2.34	2.03	1.71
$E_t^{\pi_2} > 0.50GeV$					
$\epsilon\%$	32.80	25.40	18.80	13.60	9.20
	2.56	2.25	1.94	1.65	1.36
$M_{\pi_1\pi_2} > 0.5GeV$					
$\epsilon\%$	32.00	24.80	18.60	13.60	9.20
	2.53	2.23	1.93	1.65	1.36
$E_{visible} > 130.0GeV$					
$\epsilon\%$	31.60	24.60	18.60	13.60	9.20
	2.51	2.22	1.93	1.65	1.36

Table 11. The trigger efficiency ϵ for $B_d^0 \to \pi^+\pi^-$ events at hadronic calorimeter nuclear length of 7.2 λ_{nucl} and fiber attenuation length of $\lambda_{att} = 10000$ cm. The cluster cell sizes in electromagnetic and hadronic calorimeters have been chosen as 4×4 cm^2 and 8×8 cm^2, respectively. The maximum energy deposition cluster cell was searched for hadronic calorimeter clusters and was not searched for electromagnetic ones. The following cuts $E_{preclust} \leq 0.03$ GeV, $N_{preclust} \leq 4$, $R_{isol} \geq 6$ and $\frac{E_{clust}^{EMcal}}{E_{clust}^{Hcal}} \leq 60$ have been applied during precluster and cluster finding.

$E_t^{\pi_1}(GeV) >$	1.0	1.5	2.0	2.5	3.0
$\epsilon\%$	55.40	40.40	31.40	24.20	19.00
	3.33	2.84	2.51	2.20	1.95
$E_t^{\pi_2} > 0.50GeV$					
$\epsilon\%$	38.00	28.00	21.60	16.00	12.60
	2.76	2.37	2.08	1.79	1.59
$M_{\pi_1\pi_2} > 0.5GeV$					
$\epsilon\%$	37.00	27.20	21.40	15.80	12.60
	2.72	2.33	2.07	1.78	1.59
$E_{visible} > 130.0GeV$					
$\epsilon\%$	36.20	26.80	21.20	15.80	12.60
	2.69	2.32	2.06	1.78	1.59

Table 12. The trigger efficiency for $B_d^0 \to \pi^+\pi^-$ events at hadronic calorimeter nuclear length of 3.5 λ_{nucl} and fiber attenuation length of $\lambda_{att} = 150$ cm. The standard cuts $E_t^{\pi_2} > 0.5$ GeV, $M_{\pi_1\pi_2} > 0.5$ GeV, $E_{visible} > 130$ GeV have been applied too. Moreover the following cuts $E_{preclust} \leq 0.03$ GeV, $N_{preclust} \leq 4$, $R_{isol} \geq 6$ and $\frac{E_{clust}^{EMcal}}{E_{clust}^{Hcal}} \leq 60$ have been applied during precluster and cluster finding.

$E_t^{\pi_1}(GeV) >$	1.0	1.5	2.0	2.5	3.0
ϵ_1 %	37.40	28.20	22.00	16.80	12.80
	2.73	2.38	2.10	1.83	1.60
ϵ_2 %	35.40	26.20	20.20	15.40	11.60
	2.66	2.29	2.01	1.75	1.52
ϵ_3 %	25.00	18.40	12.60	8.60	6.00
	2.24	1.92	1.59	1.31	1.10
ϵ_4 %	43.20	32.00	24.60	19.80	14.80
	2.94	2.53	2.22	1.99	1.72
ϵ_5 %	6.80	3.40	2.20	1.00	0.60
	1.17	0.82	0.66	0.45	0.35

Table 13. The efficiency ϵ to register a minimum bias event as a $B_d^0 \to \pi^+\pi^-$ event candidate at hadronic calorimeter nuclear length of 3.5 λ_{nucl} and fiber attenuation length of $\lambda_{att} = 150$ cm. The standard cuts $E_t^{\pi_2} > 0.5$ GeV, $M_{\pi_1\pi_2} > 0.5$ GeV, $E_{visible} > 130$ GeV have been applied too. Moreover the following cuts $E_{preclust} \leq 0.03$ GeV, $N_{preclust} \leq 4$, $R_{isol} \geq 6$ and $\frac{E_{clust}^{EMcal}}{E_{clust}^{Hcal}} \leq 60$ have been applied during precluster and cluster finding.

$E_t^{\pi_1}(GeV) >$	1.0	1.5	2.0	2.5	3.0
ϵ_1 %	9.23	3.63	1.47	0.50	0.23
	0.56	0.35	0.22	0.13	0.09
ϵ_2 %	8.07	2.90	1.40	0.37	0.20
	0.52	0.31	0.22	0.11	0.08
ϵ_3 %	4.33	1.60	0.53	0.30	0.17
	0.38	0.23	0.13	0.10	0.08
ϵ_4 %	10.53	4.30	1.70	0.60	0.27
	0.59	0.38	0.24	0.14	0.09
ϵ_5 %	0.80	0.10	0.07	0.07	0.07
	0.16	0.06	0.05	0.05	0.05

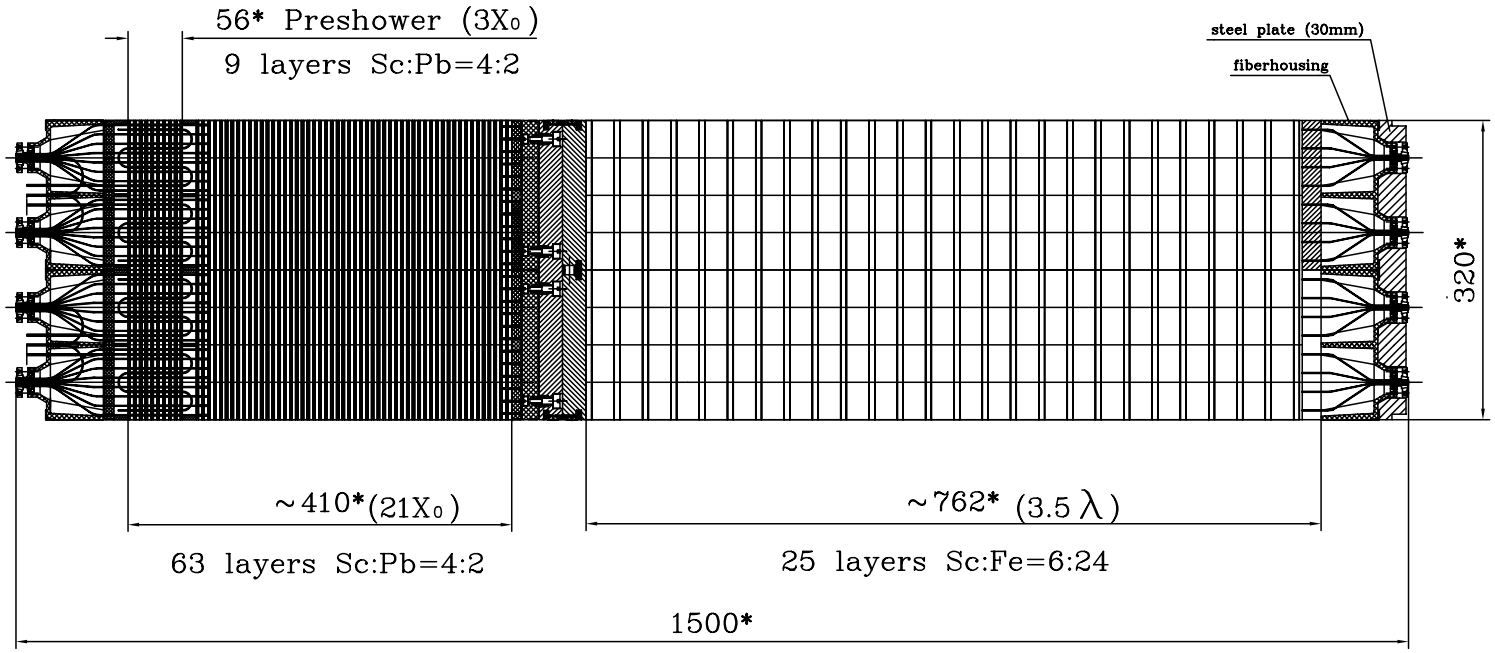

Fig. 1

Combined calorimeter module.

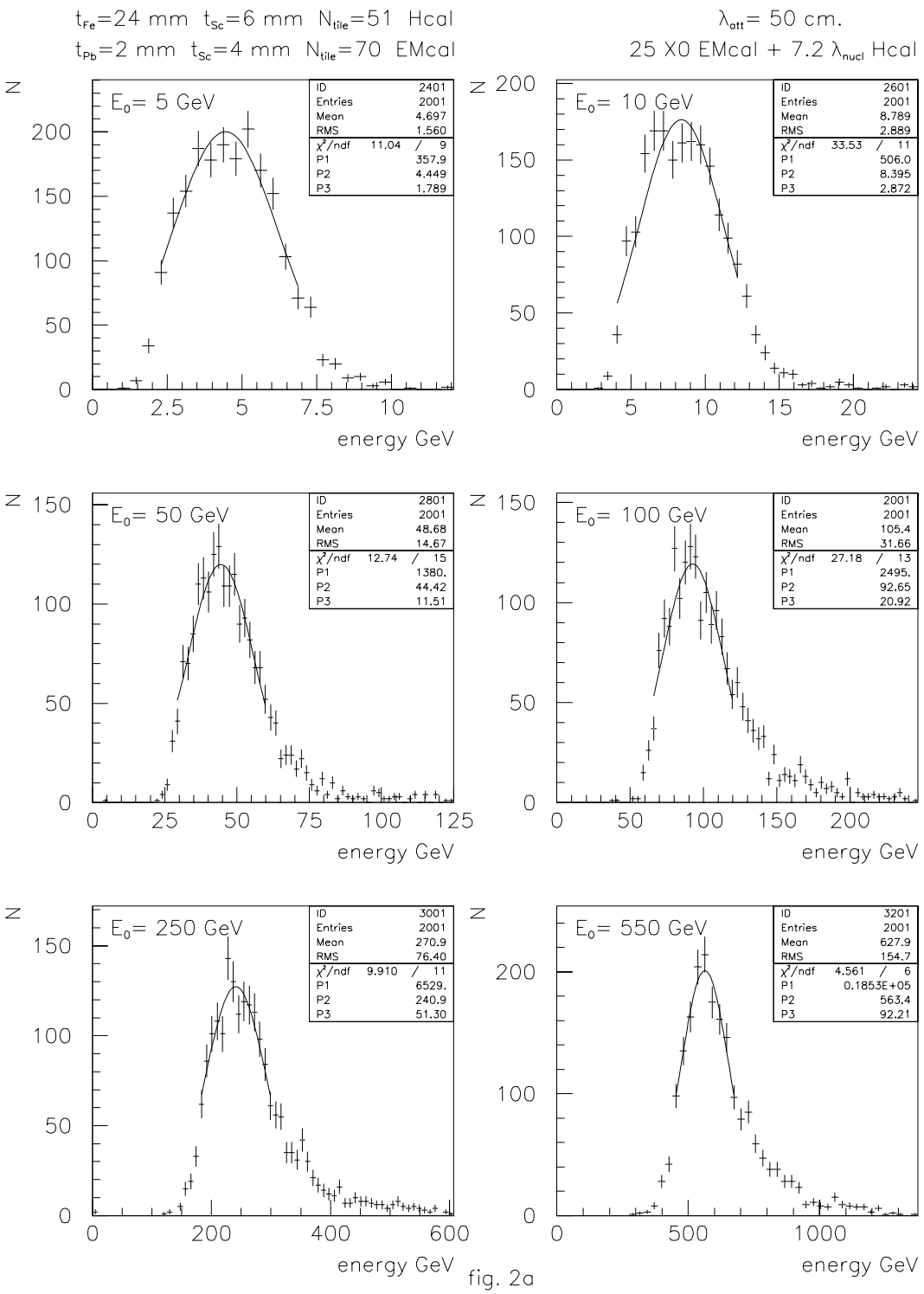

fig. 2a

Distributions on the reconstruction energy of π^+-mesons having initial momentum of 5, 10, 50, 100, 250, 550 GeV/c for hadronic calorimeter nuclear length $\lambda_{Hcal} = 7.2\ \lambda_{nucl}$ and fiber attenuation length $\lambda_{att} = 50$ cm. The results of fitting these distributions to Gaussian by means of the Least Square Method in a region of the peak are shown with a solid curve.

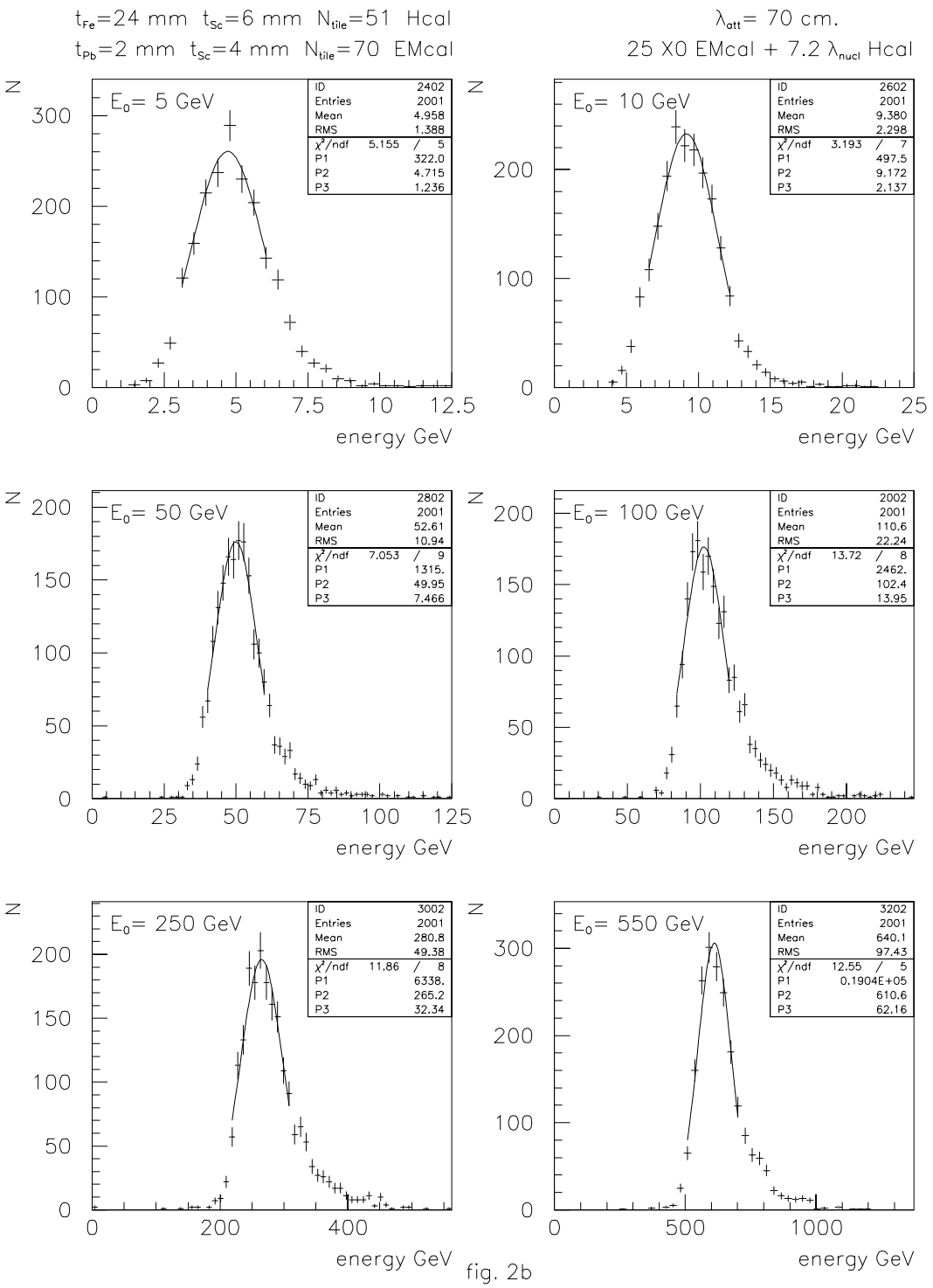

fig. 2b

Distributions on the reconstruction energy of π^+-mesons having initial momentum of 5, 10, 50, 100, 250, 550 GeV/c for hadronic calorimeter nuclear length $\lambda_{Hcal} = 7.2\ \lambda_{nucl}$ and fiber attenuation length $\lambda_{att} = 70$ cm. The results of fitting these distributions to Gaussian by means of the Least Square Method in a region of the peak are shown with a solid curve.

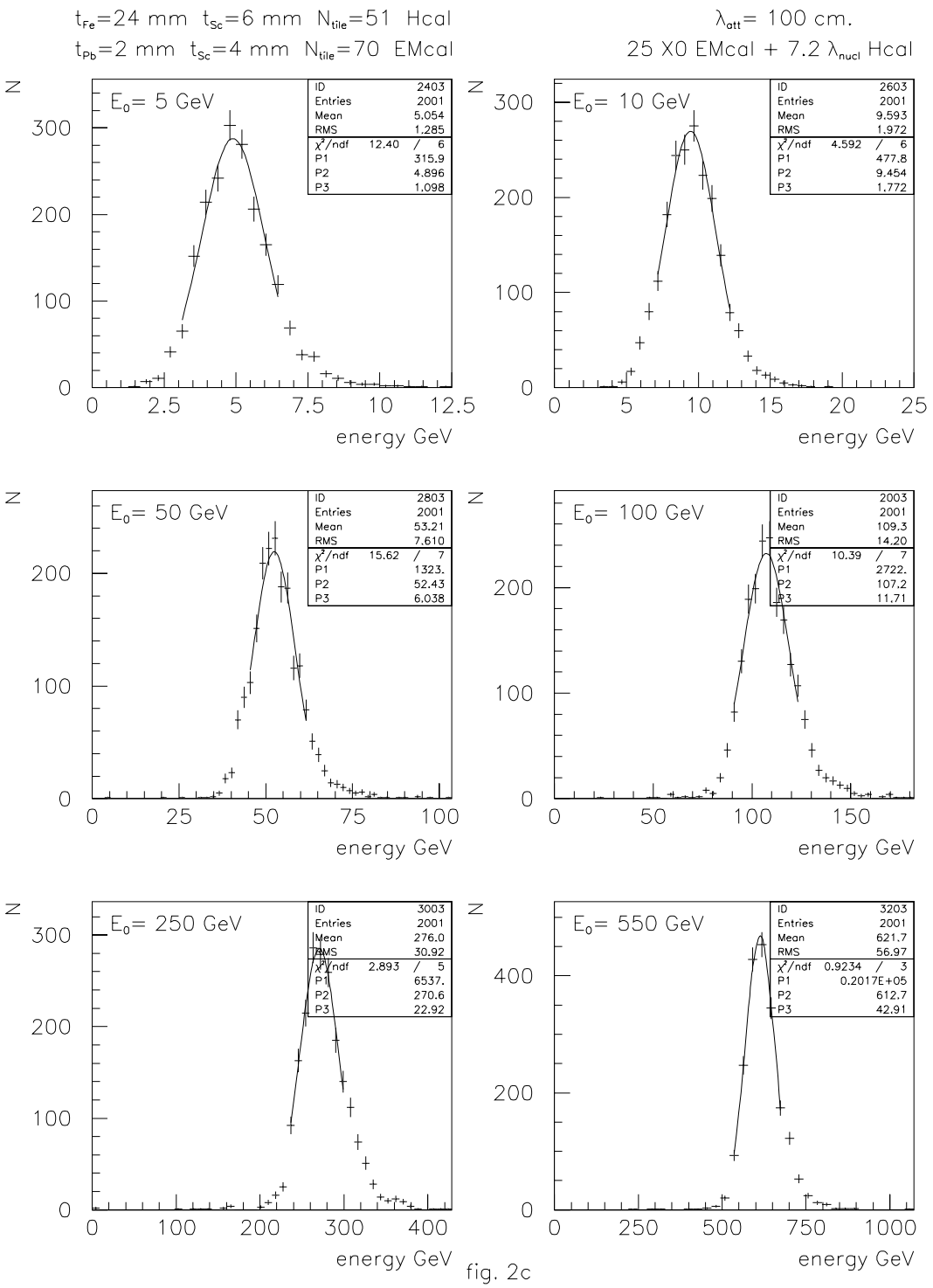

fig. 2c

Distributions on the reconstruction energy of π^+-mesons having initial momentum of 5, 10, 50, 100, 250, 550 GeV/c for hadronic calorimeter nuclear length $\lambda_{Hcal} = 7.2\ \lambda_{nucl}$ and fiber attenuation length $\lambda_{att} = 100$ cm. The results of fitting these distributions to Gaussian by means of the Least Square Method in a region of the peak are shown with a solid curve.

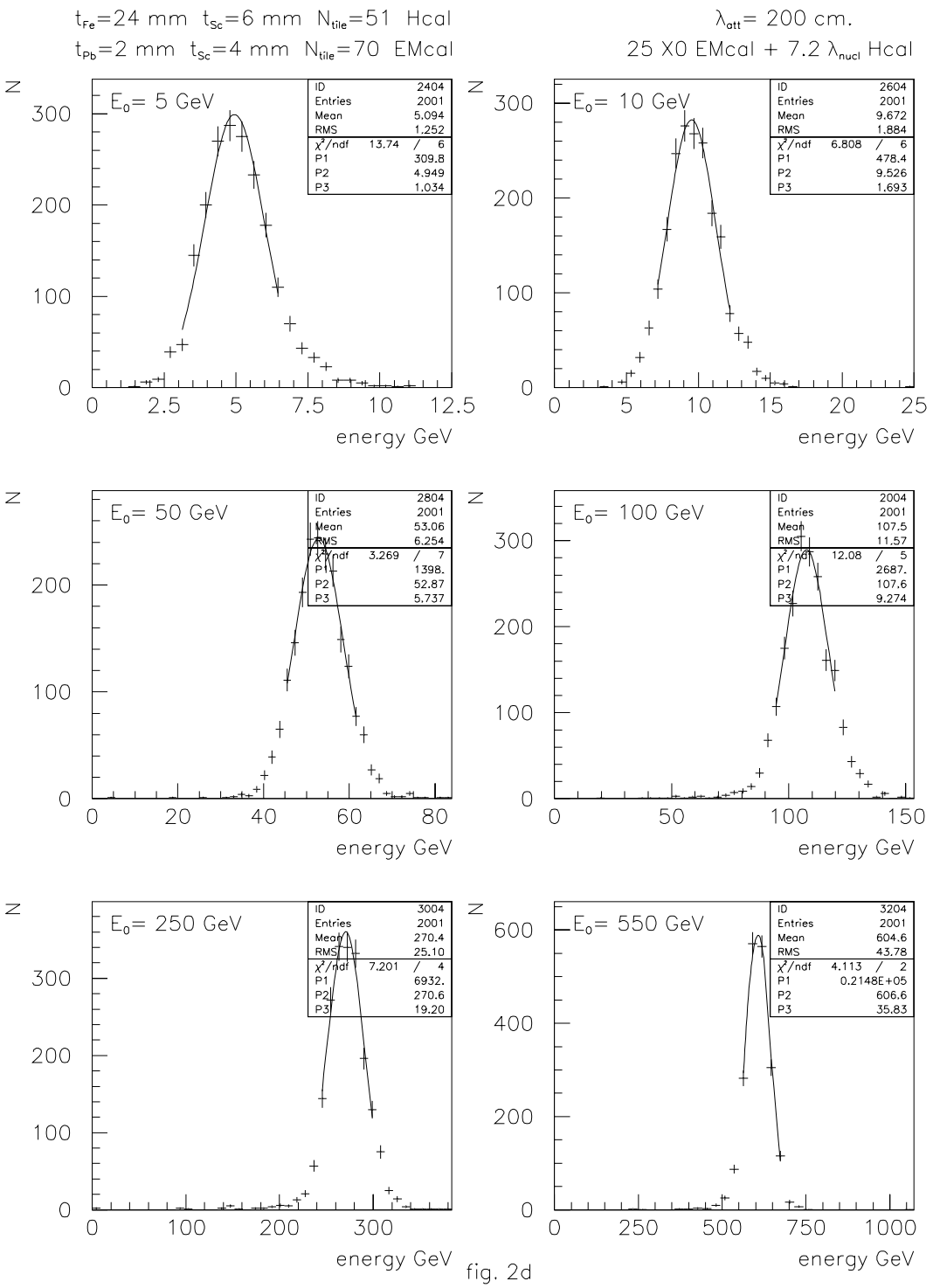

fig. 2d

Distributions on the reconstruction energy of π^+-mesons having initial momentum of 5, 10, 50, 100, 250, 550 GeV/c for hadronic calorimeter nuclear length $\lambda_{Hcal} = 7.2\ \lambda_{nucl}$ and fiber attenuation length $\lambda_{att} = 200$ cm. The results of fitting these distributions to Gaussian by means of the Least Square Method in a region of the peak are shown with a solid curve.

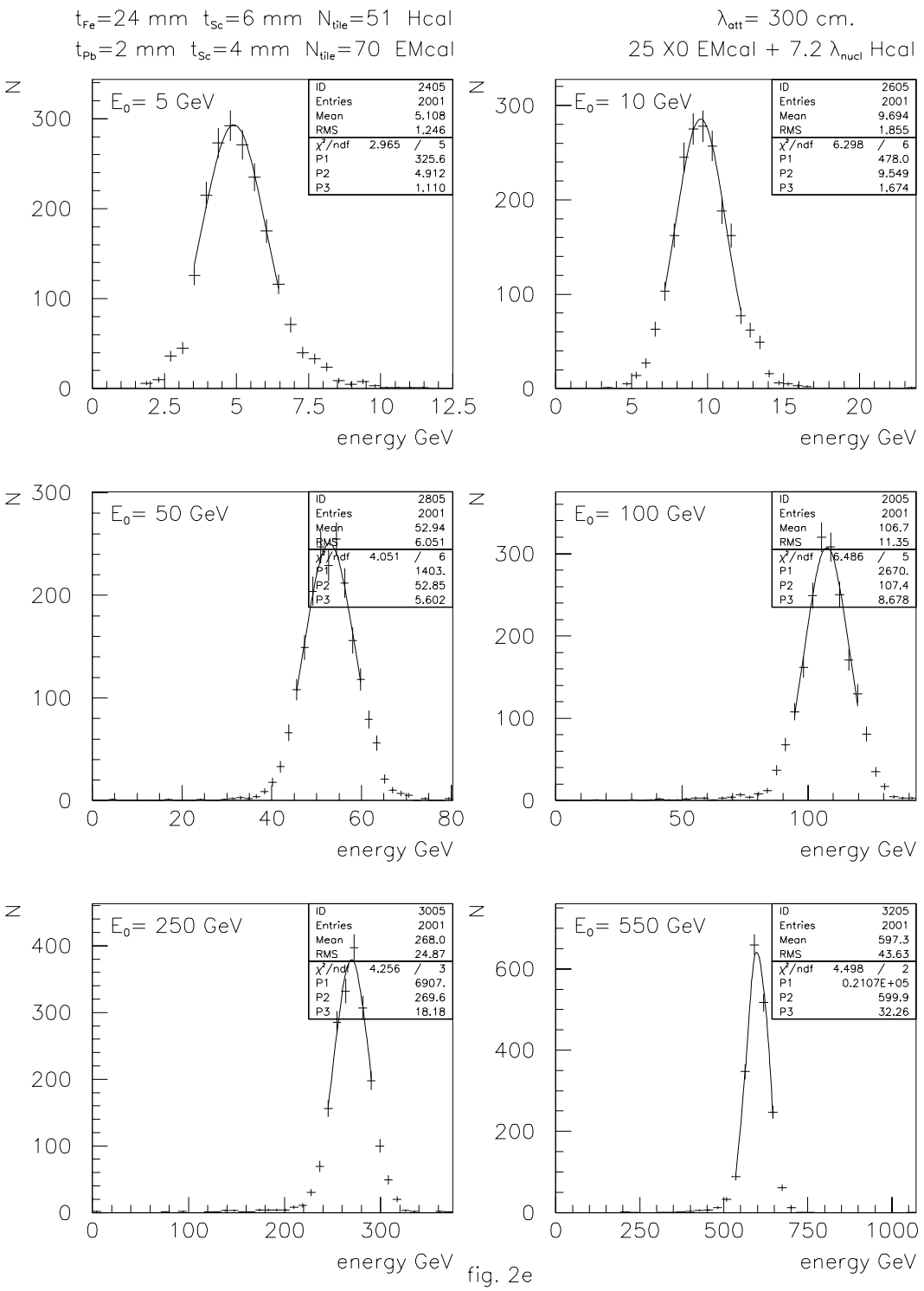

fig. 2e

Distributions on the reconstruction energy of π^+-mesons having initial momentum of 5, 10, 50, 100, 250, 550 GeV/c for hadronic calorimeter nuclear length $\lambda_{Hcal} = 7.2\ \lambda_{nucl}$ and fiber attenuation length $\lambda_{att} = 300$ cm. The results of fitting these distributions to Gaussian by means of the Least Square Method in a region of the peak are shown with a solid curve.

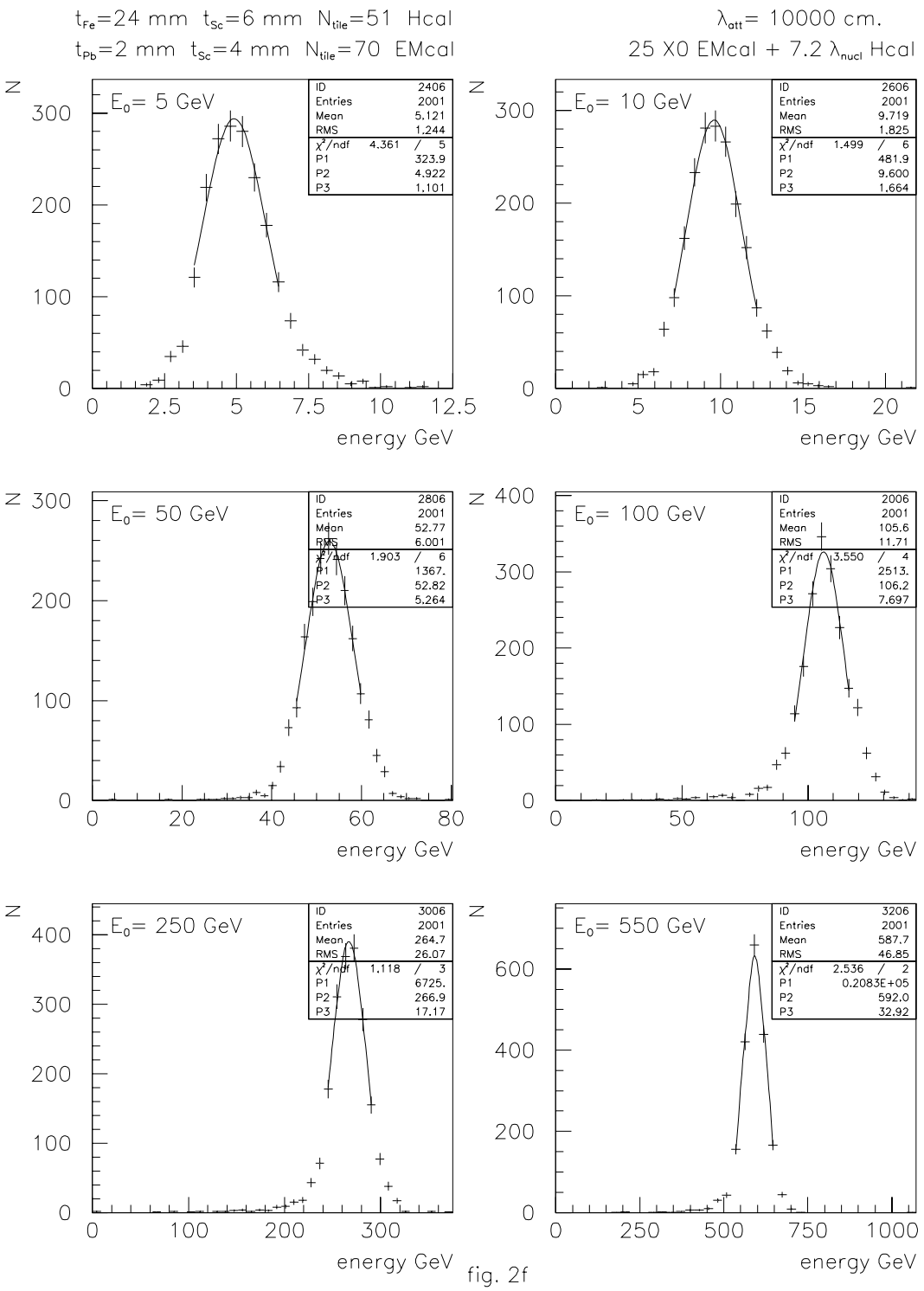

fig. 2f

Distributions on the reconstruction energy of π^+-mesons having initial momentum of 5, 10, 50, 100, 250, 550 GeV/c for hadronic calorimeter nuclear length $\lambda_{Hcal} = 7.2\ \lambda_{nucl}$ and fiber attenuation length $\lambda_{att} = 10000$ cm. The results of fitting these distributions to Gaussian by means of the Least Square Method in a region of the peak are shown with a solid curve.

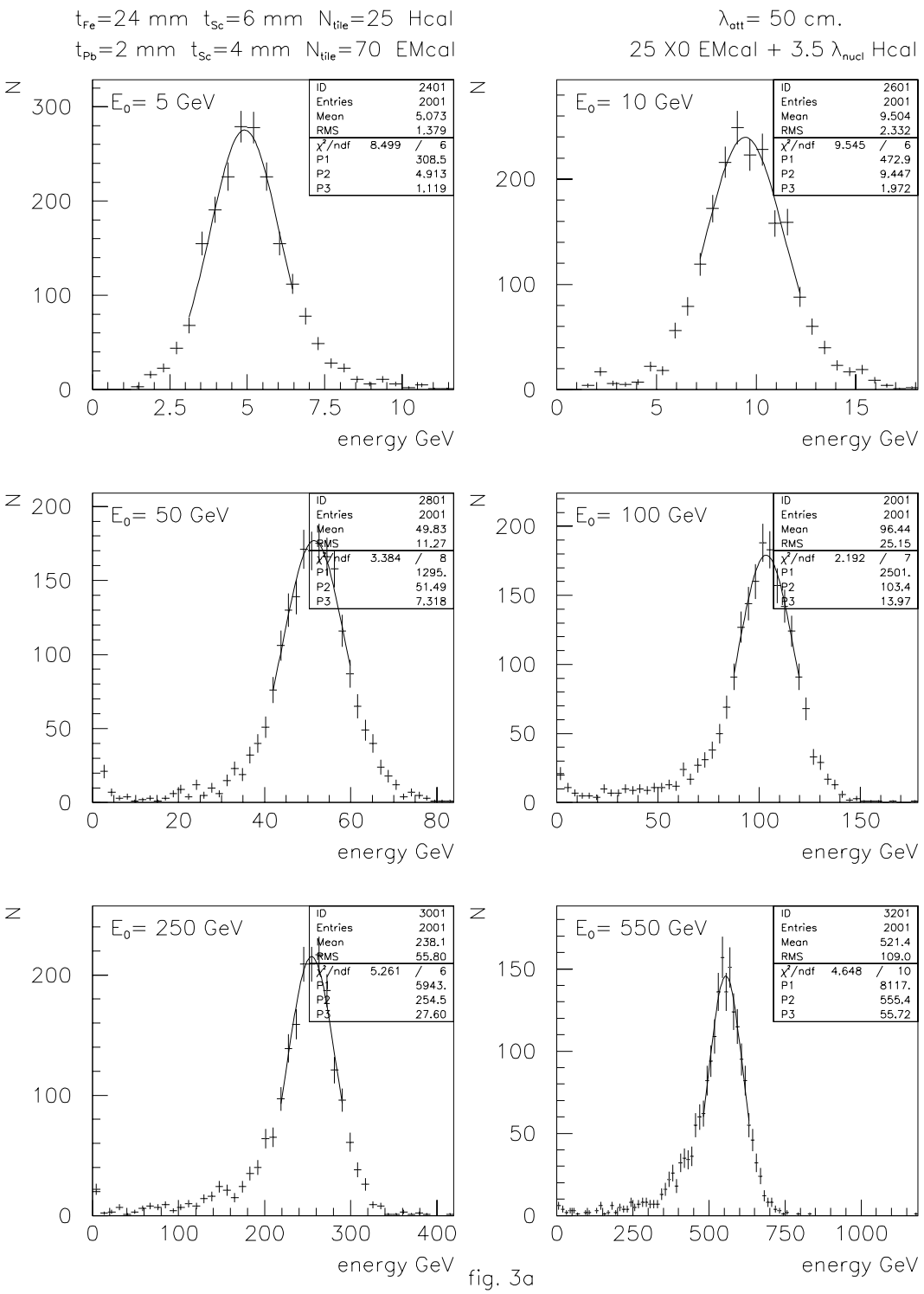

fig. 3a

Distributions on the reconstruction energy of π^+-mesons having initial momentum of 5, 10, 50, 100, 250, 550 GeV/c for hadronic calorimeter nuclear length $\lambda_{Hcal} = 3.5\ \lambda_{nucl}$ and fiber attenuation length $\lambda_{att} = 50$ cm. The results of fitting these distributions to Gaussian by means of the Least Square Method in a region of the peak are shown with a solid curve.

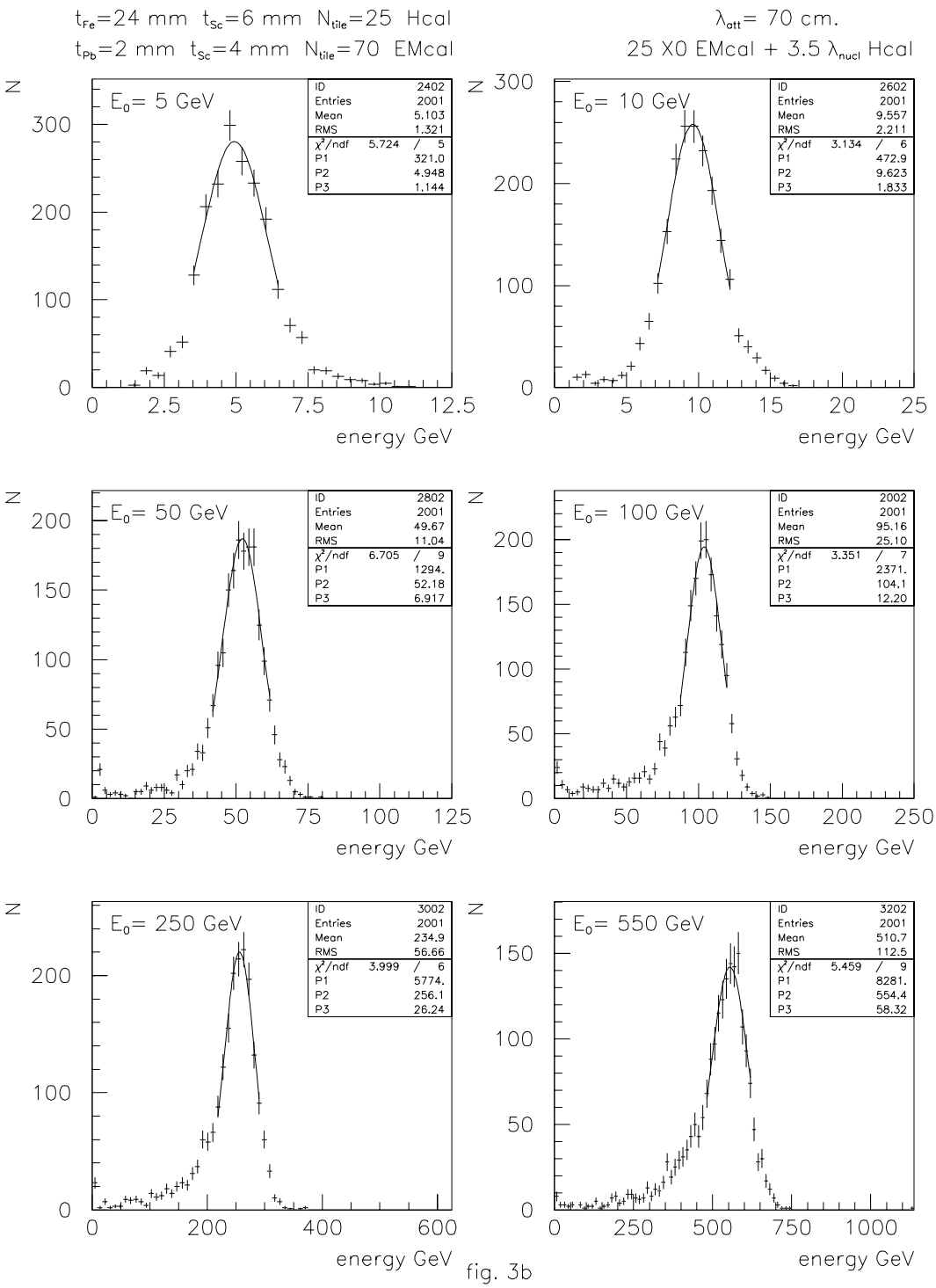

fig. 3b

Distributions on the reconstruction energy of π^+-mesons having initial momentum of 5, 10, 50, 100, 250, 550 GeV/c for hadronic calorimeter nuclear length $\lambda_{Hcal} = 3.5\ \lambda_{nucl}$ and fiber attenuation length $\lambda_{att} = 70$ cm. The results of fitting these distributions to Gaussian by means of the Least Square Method in a region of the peak are shown with a solid curve.

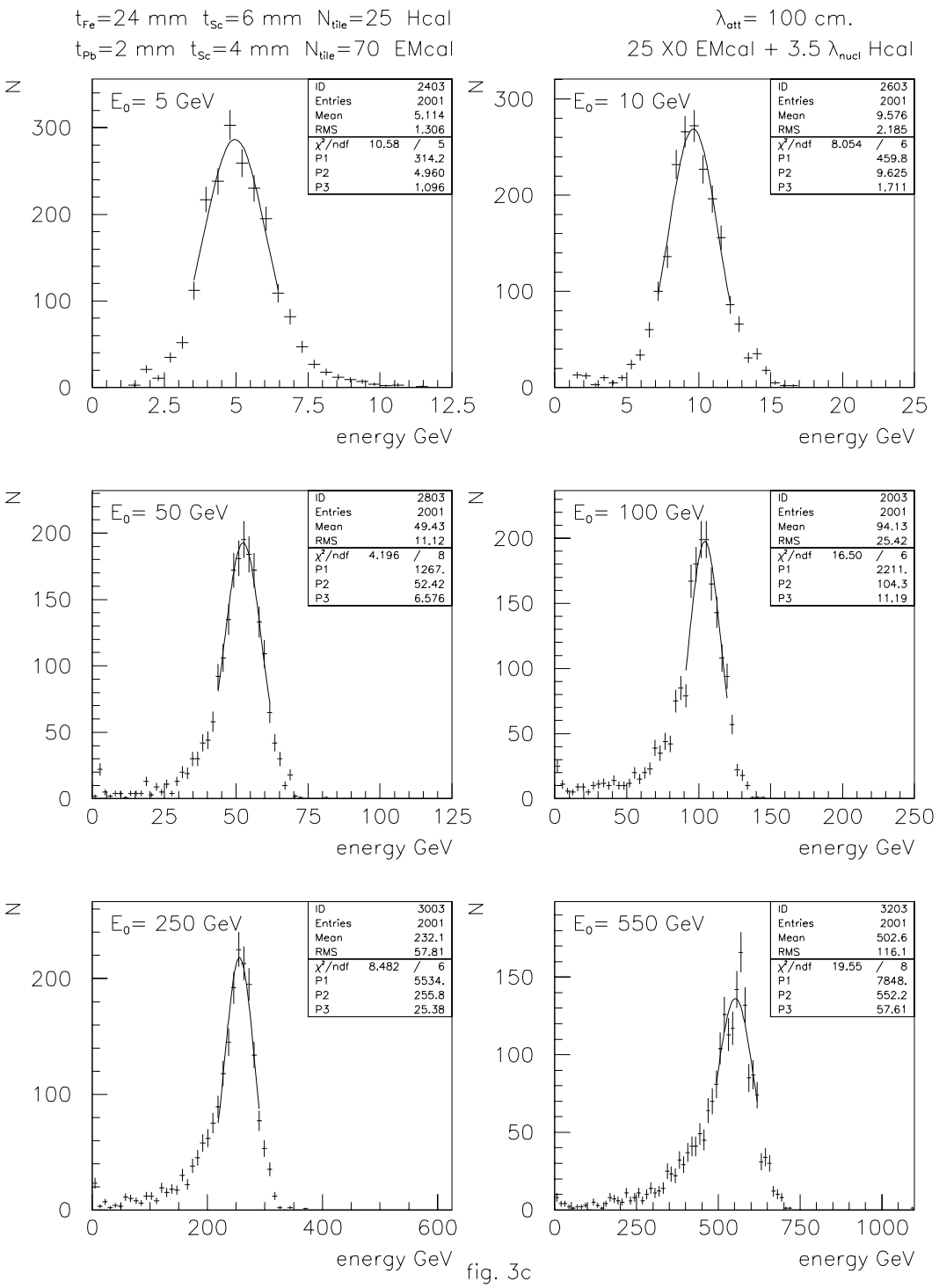

fig. 3c

Distributions on the reconstruction energy of π^+-mesons having initial momentum of 5, 10, 50, 100, 250, 550 GeV/c for hadronic calorimeter nuclear length $\lambda_{Hcal} = 3.5\ \lambda_{nucl}$ and fiber attenuation length $\lambda_{att} = 100$ cm. The results of fitting these distributions to Gaussian by means of the Least Square Method in a region of the peak are shown with a solid curve.

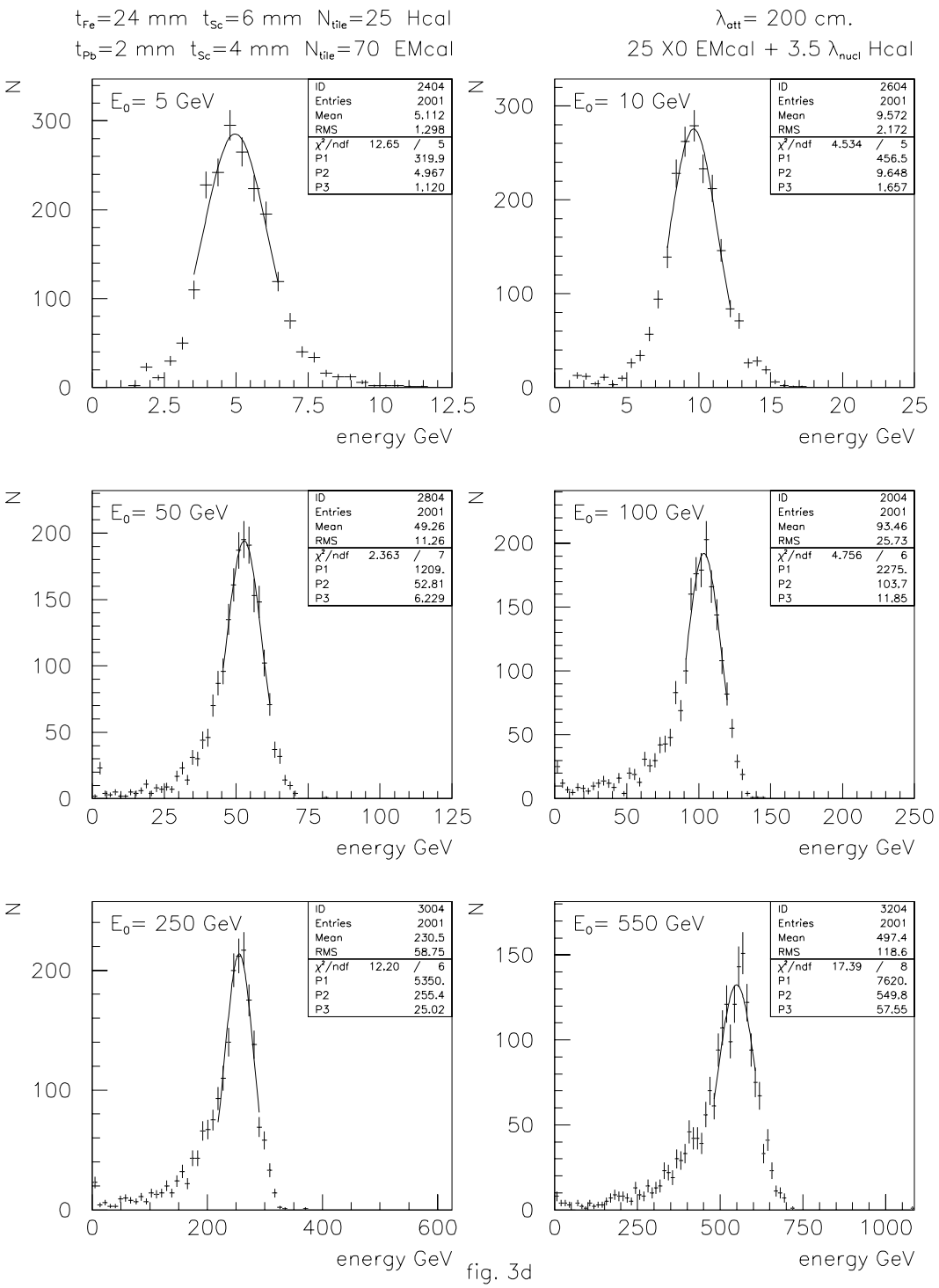

fig. 3d

Distributions on the reconstruction energy of π^+-mesons having initial momentum of 5, 10, 50, 100, 250, 550 GeV/c for hadronic calorimeter nuclear length $\lambda_{Hcal} = 3.5\ \lambda_{nucl}$ and fiber attenuation length $\lambda_{att} = 200$ cm. The results of fitting these distributions to Gaussian by means of the Least Square Method in a region of the peak are shown with a solid curve.

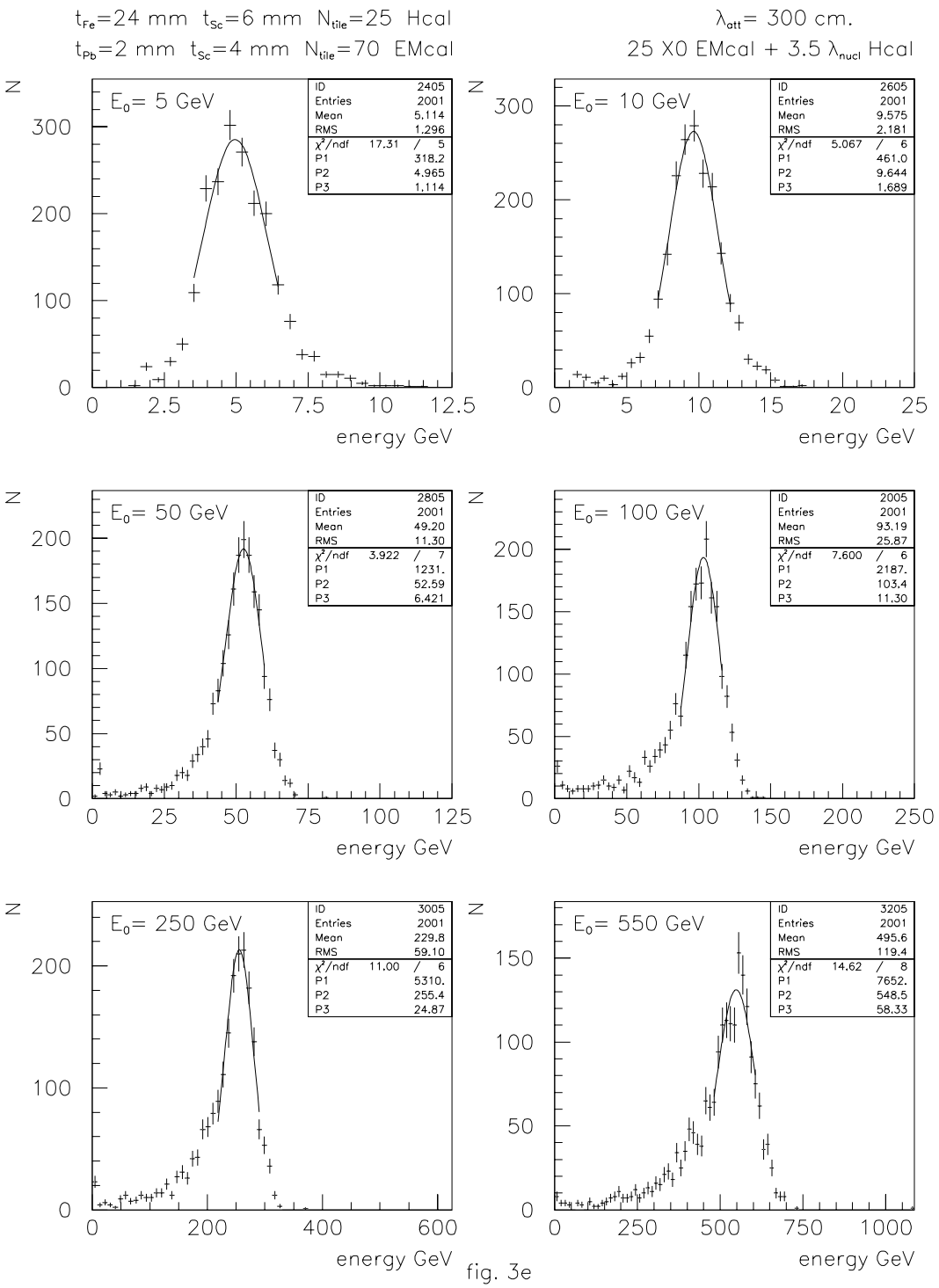

fig. 3e

Distributions on the reconstruction energy of π^+-mesons having initial momentum of 5, 10, 50, 100, 250, 550 Gev/c for hadronic calorimeter nuclear length $\lambda_{Hcal} = 3.5\ \lambda_{nucl}$ and fiber attenuation length $\lambda_{att} = 300$ cm. The results of fitting these distributions to Gaussian by means of the Least Square Method in a region of the peak are shown with a solid curve.

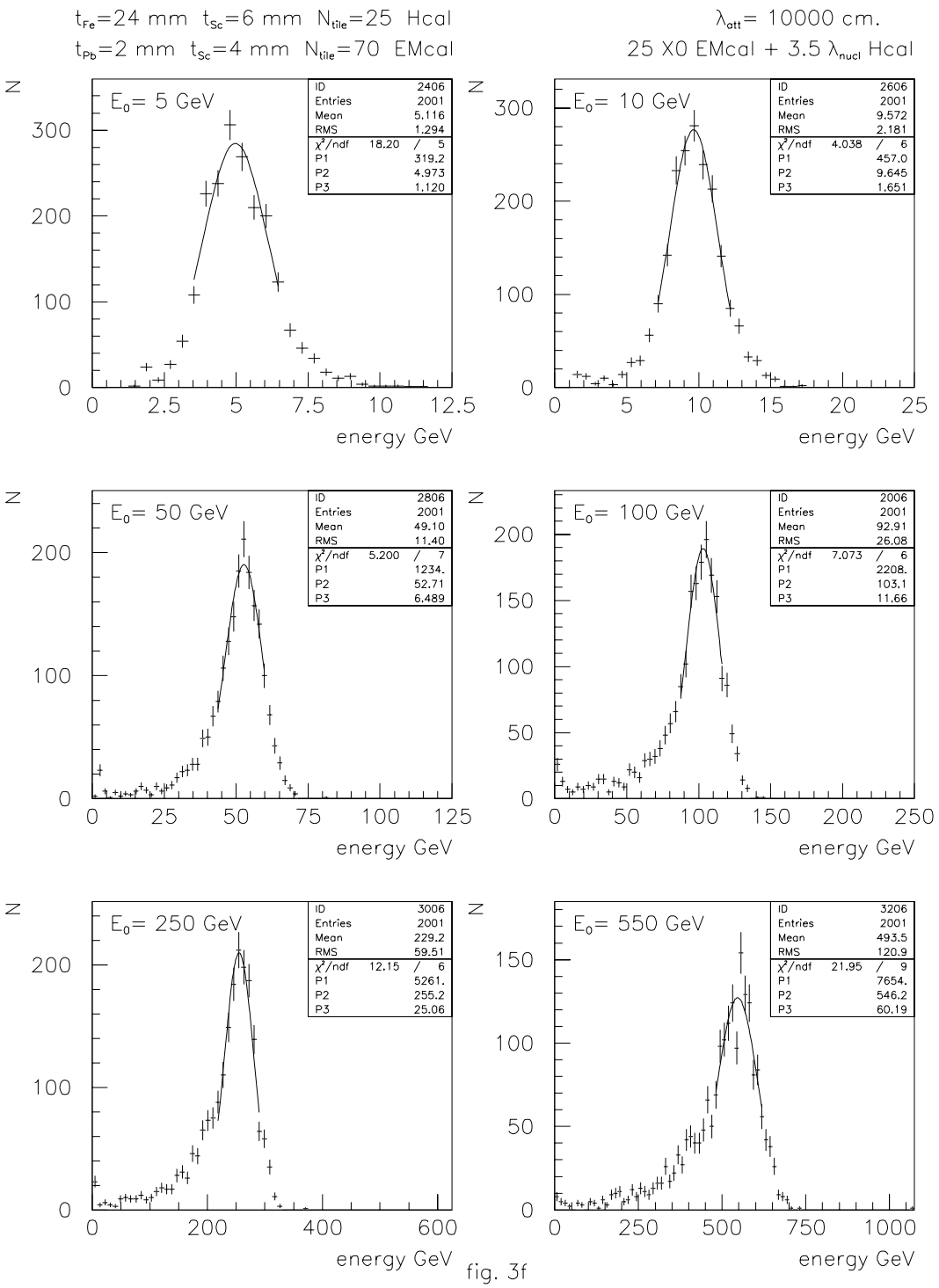

fig. 3f

Distributions on the reconstruction energy of π^+-mesons having initial momentum of 5, 10, 50, 100, 250, 550 GeV/c for hadronic calorimeter nuclear length $\lambda_{Hcal} = 3.5\ \lambda_{nucl}$ and fiber attenuation length $\lambda_{att} = 10000$ cm. The results of fitting these distributions to Gaussian by means of the Least Square Method in a region of the peak are shown with a solid curve.

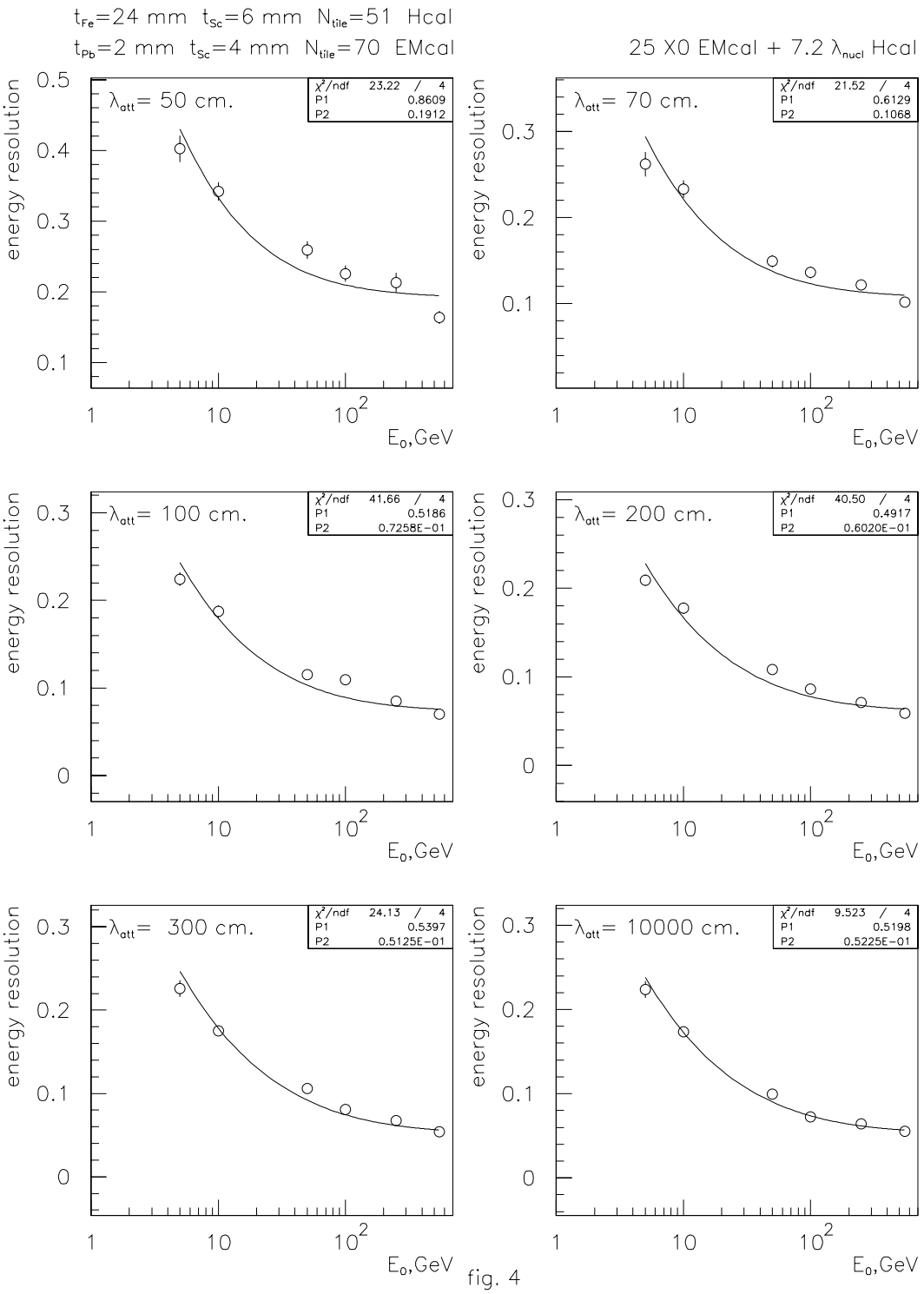

fig. 4

Dependence of the combined calorimeter energy resolution on initial pion energy E_0 for hadronic calorimeter nuclear length $\lambda_{Hcal} = 7.2\ \lambda_{nucl}$ and different values of fiber attenuation length λ_{att}. The results of fitting these Distributions by means of the Least Square Method to the function $\frac{\sigma_E}{E} = \frac{\sigma}{\sqrt{E}} \oplus C$ are shown with a solid curve.

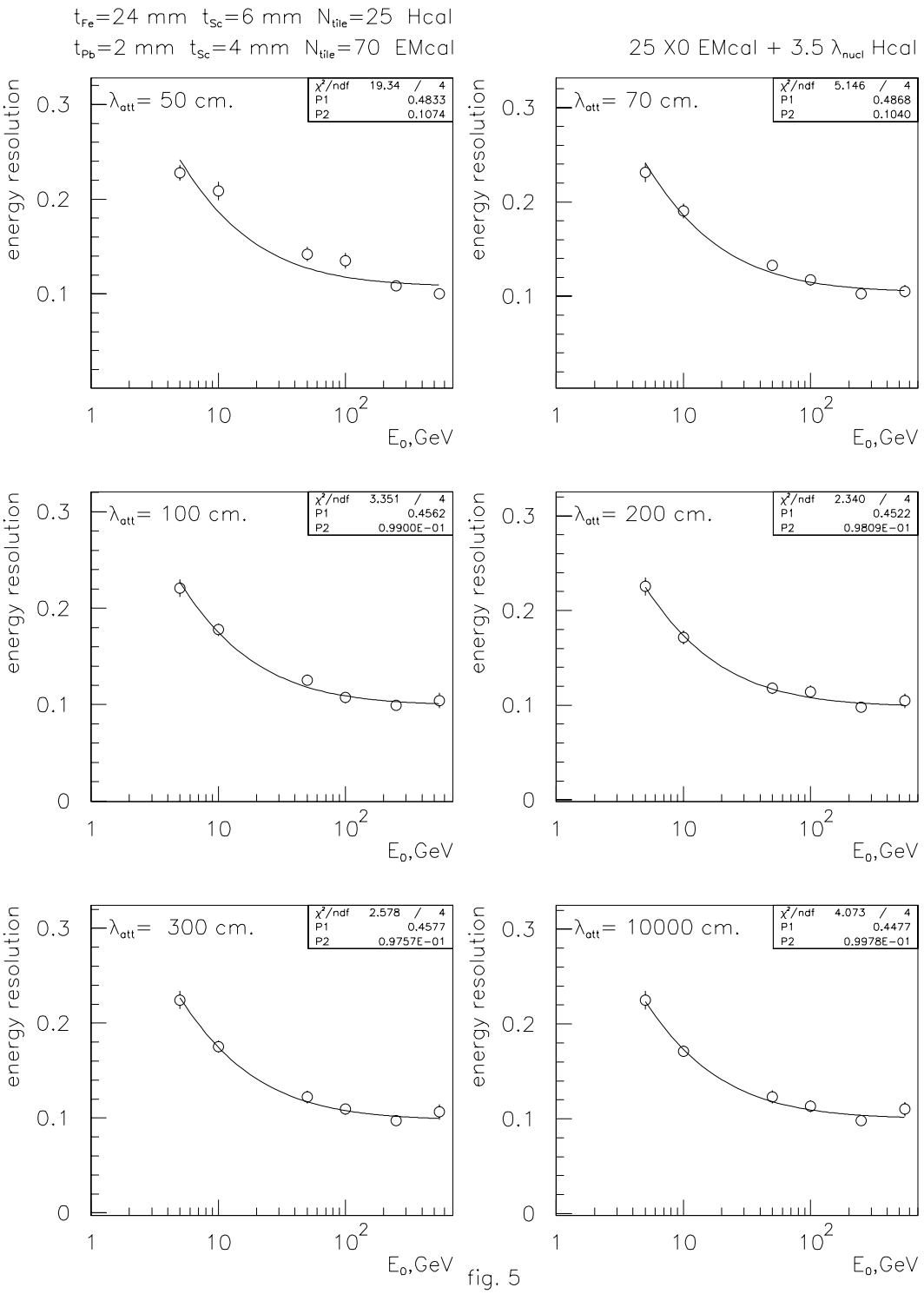

fig. 5

Dependence of the combined calorimeter energy resolution on initial pion energy E_0 for hadronic calorimeter nuclear length $\lambda_{Hcal} = 3.5\ \lambda_{nucl}$ and different values of fiber attenuation length λ_{att}. The results of fitting these Distributions by means of the Least Square Method to the function $\frac{\sigma_E}{E} = \frac{\sigma}{\sqrt{E}} \oplus C$ are shown with a solid curve.

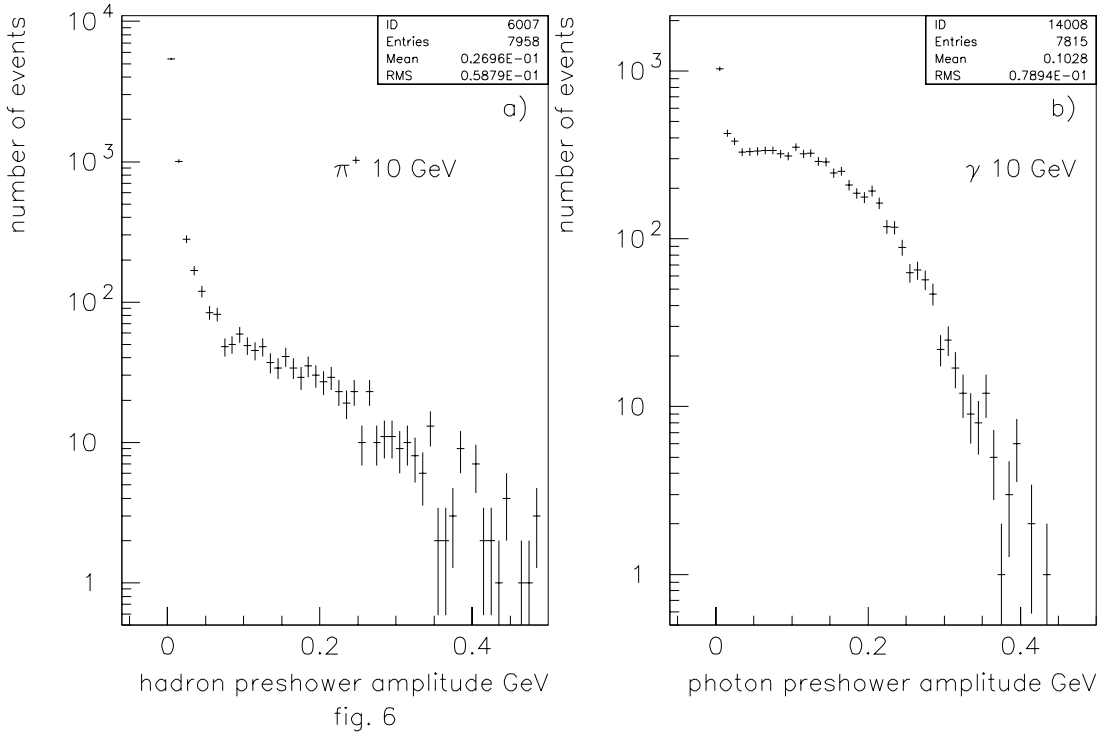

fig. 6

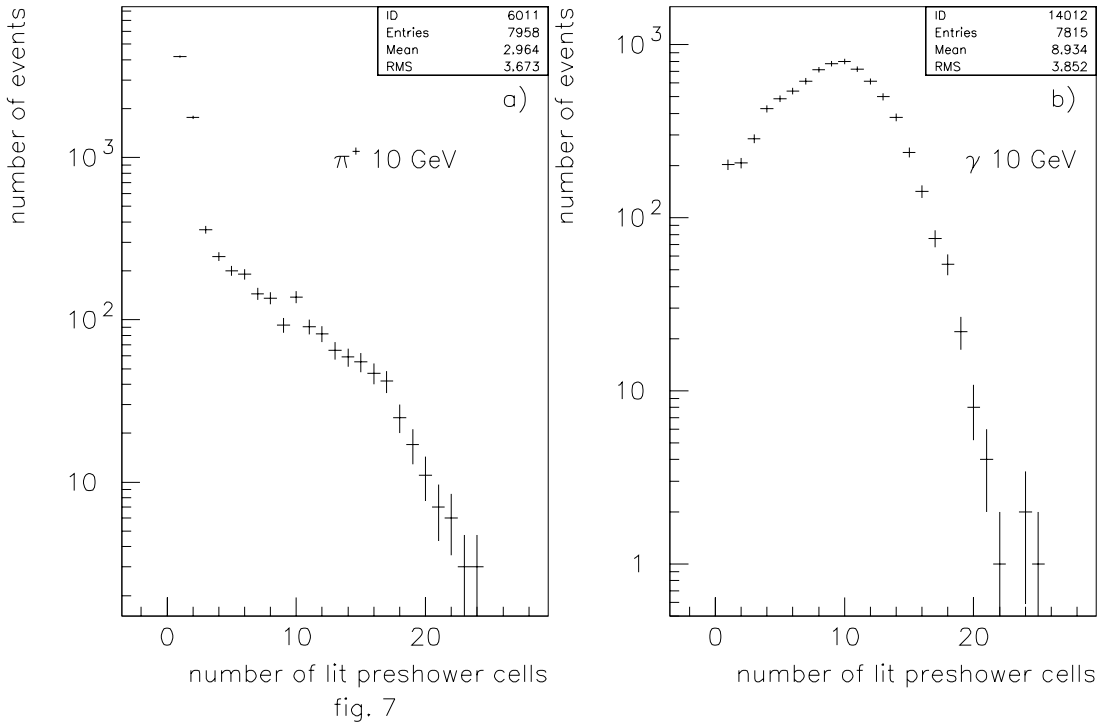

fig. 7

Fig.6a. Distribution on the energy deposited in the preshower by 10 GeV/c π^+.

Fig.6b. Distribution on the energy deposited in the preshower by 10 GeV/c γ.

Fig.7a. Distribution on the number of preshower cells lit by 10 GeV/c π^+.

Fig.7b. Distribution on the number of preshower cells lit by 10 GeV/c γ.

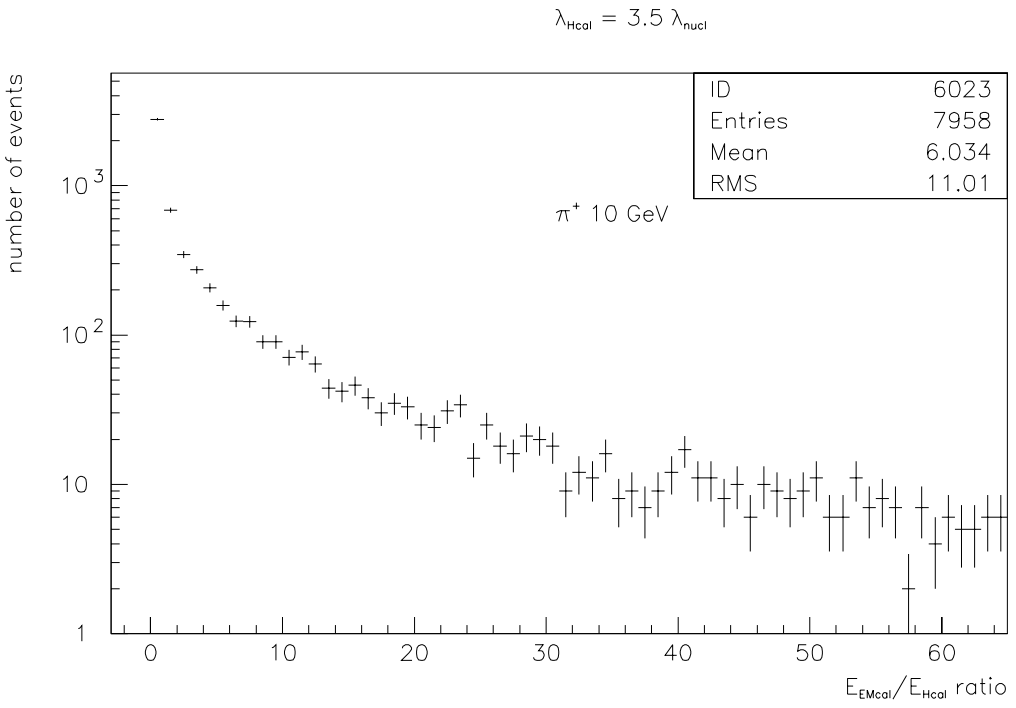

fig. 8

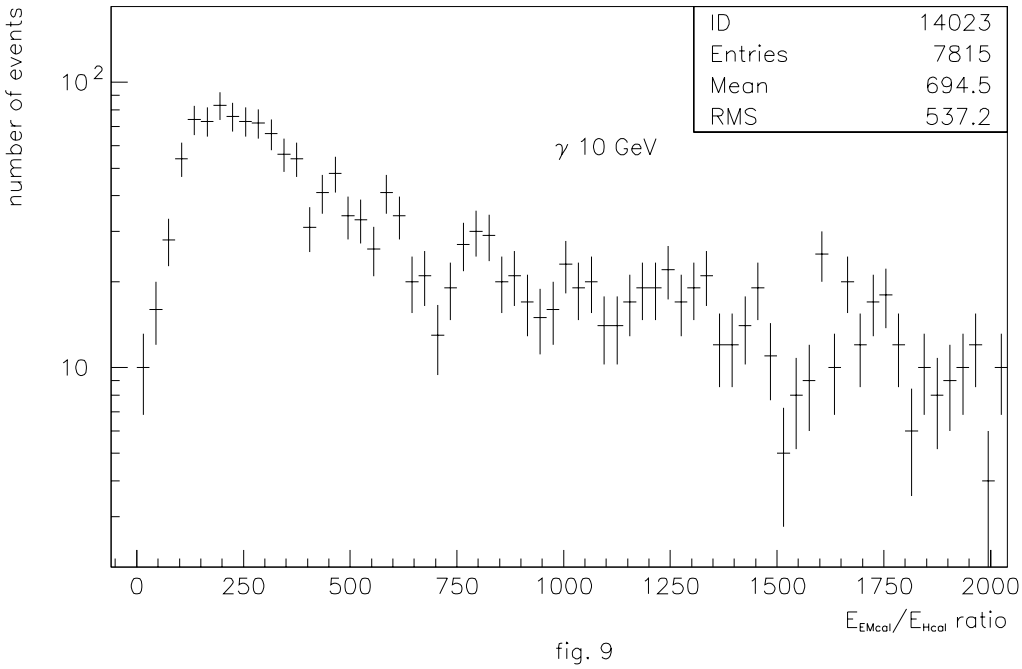

fig. 9

Fig.8. Distribution on the ratio $\beta = \frac{E_{EMcal}}{E_{Hcal}}$ of an energy deposited by 10 GeV/c π^+ in the electromagnetic calorimeter to the hadronic one for hadronic calorimeter nuclear length $\lambda_{Hcal} = 3.5\ \lambda_{nucl}$ and fiber attenuation length $\lambda_{att} = 150$ cm.

Fig.9. Distribution on the ratio $\beta = \frac{E_{EMcal}}{E_{Hcal}}$ of an energy deposited by 10 GeV/c γ in the electromagnetic calorimeter to the hadronic one for hadronic calorimeter nuclear length $\lambda_{Hcal} = 3.5\ \lambda_{nucl}$ and fiber attenuation length $\lambda_{att} = 150$ cm.

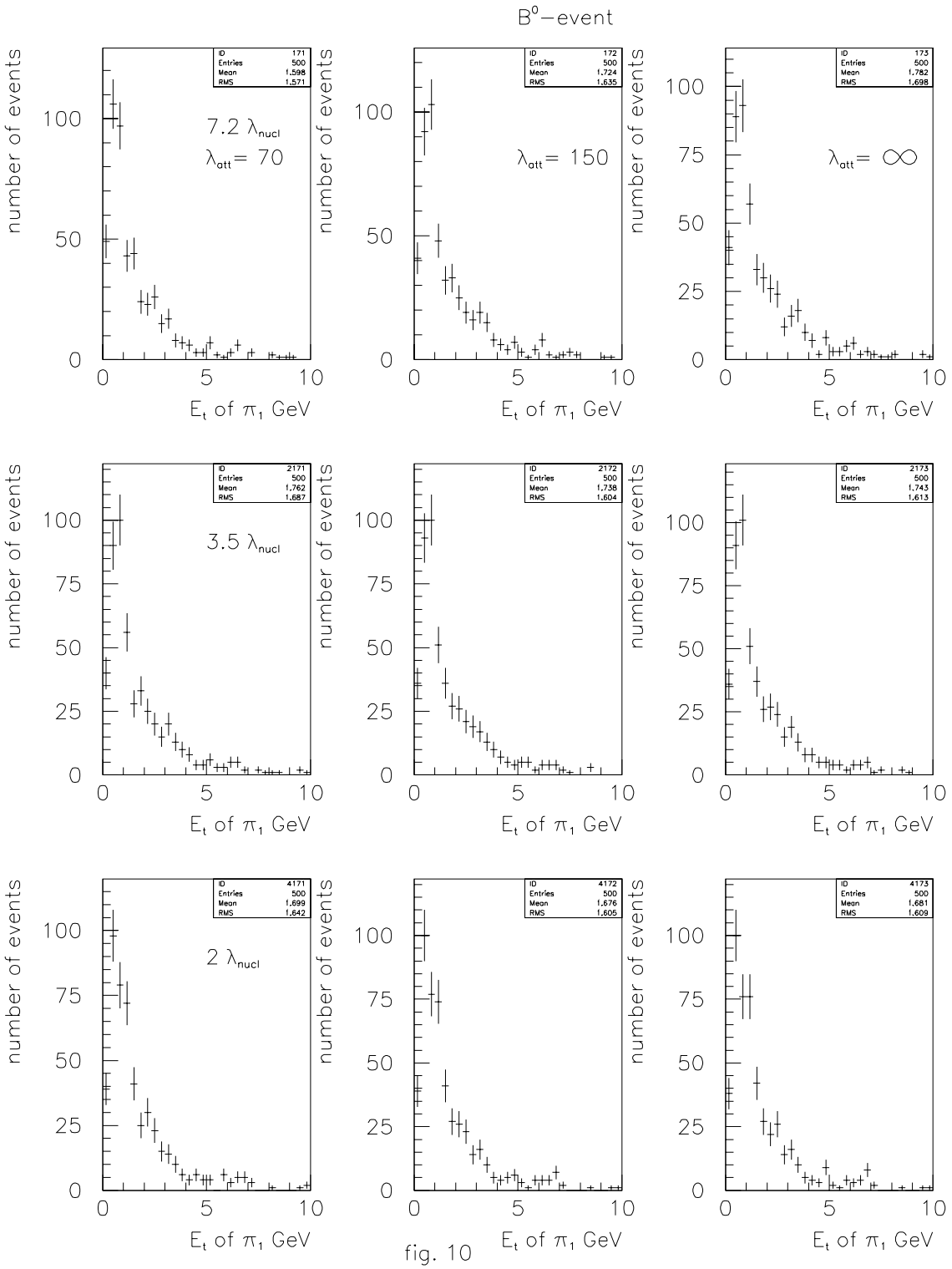

fig. 10

Distributions on the first pion transverse energy $E_t^{\pi_1}$ for different fiber attenuation length values λ_{att} and different values of hadronic calorimeter nuclear length for B_d^0 events.

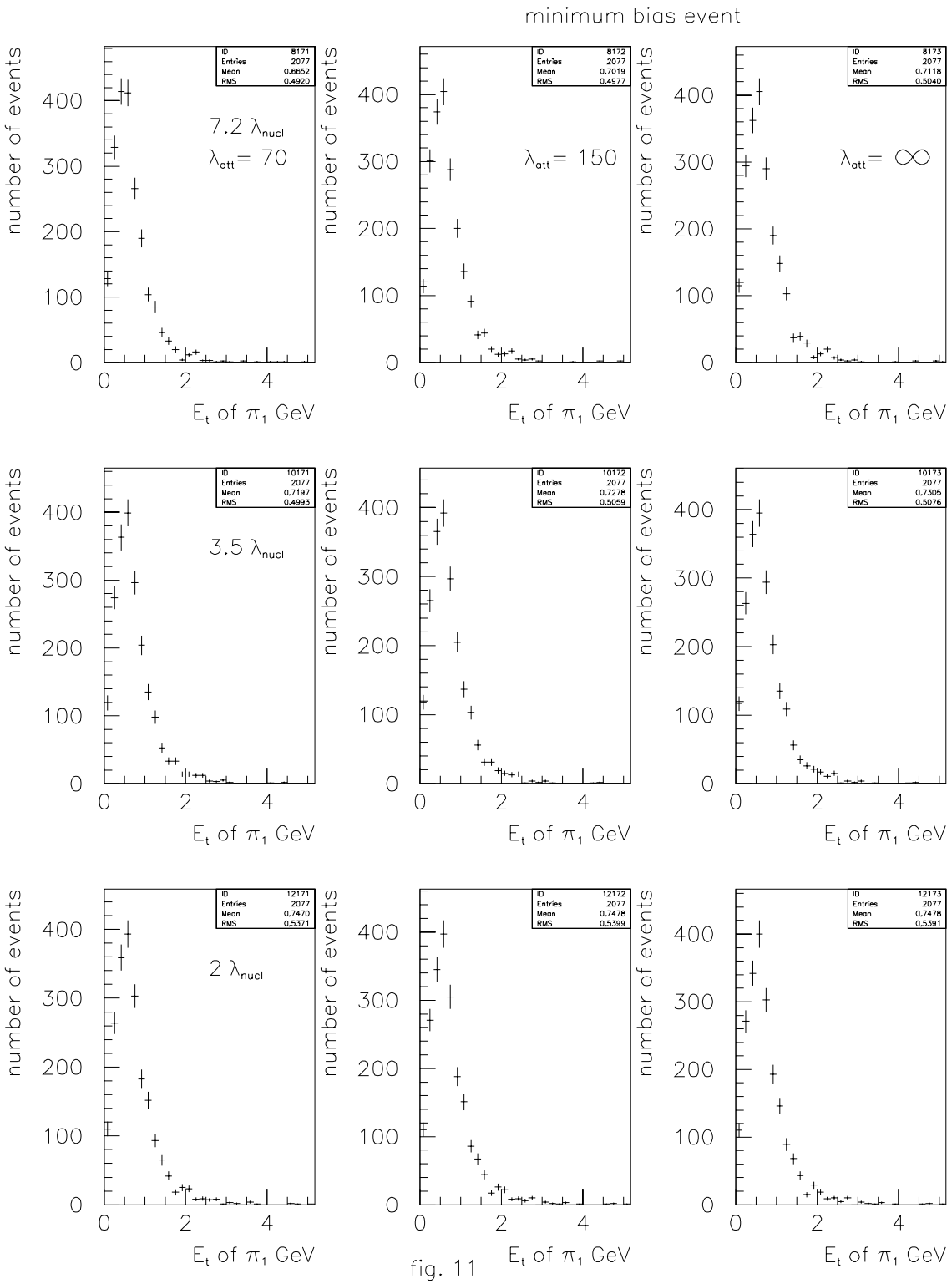

fig. 11

Distributions on the first pion transverse energy $E_t^{\pi_1}$ for different fiber attenuation length values λ_{att} and different values of hadronic calorimeter nuclear length for minimum bias events.

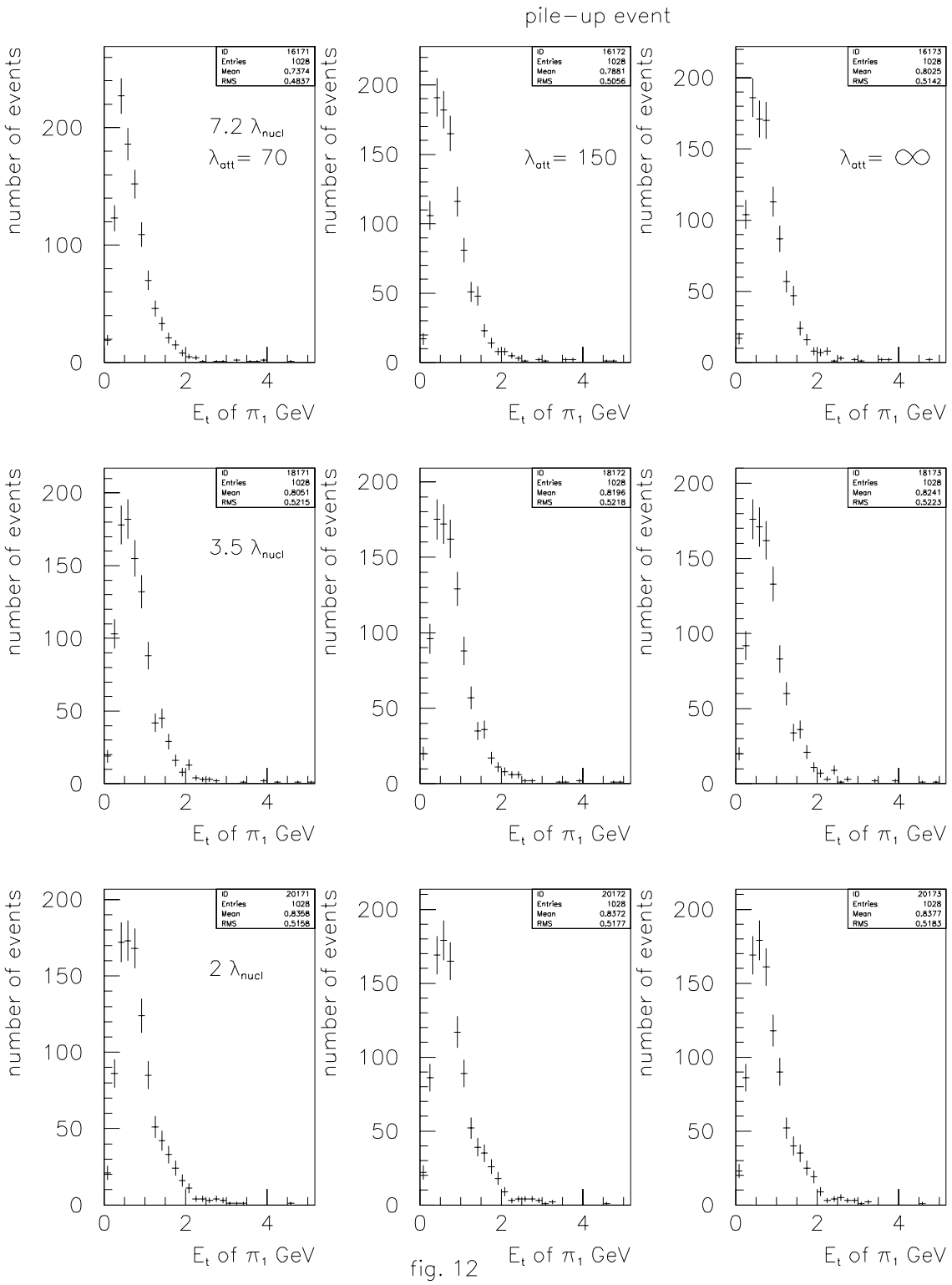

fig. 12

Distributions on the first pion transverse energy $E_t^{\pi_1}$ for different fiber attenuation length values λ_{att} and different values of hadronic calorimeter nuclear length for pile-up events.

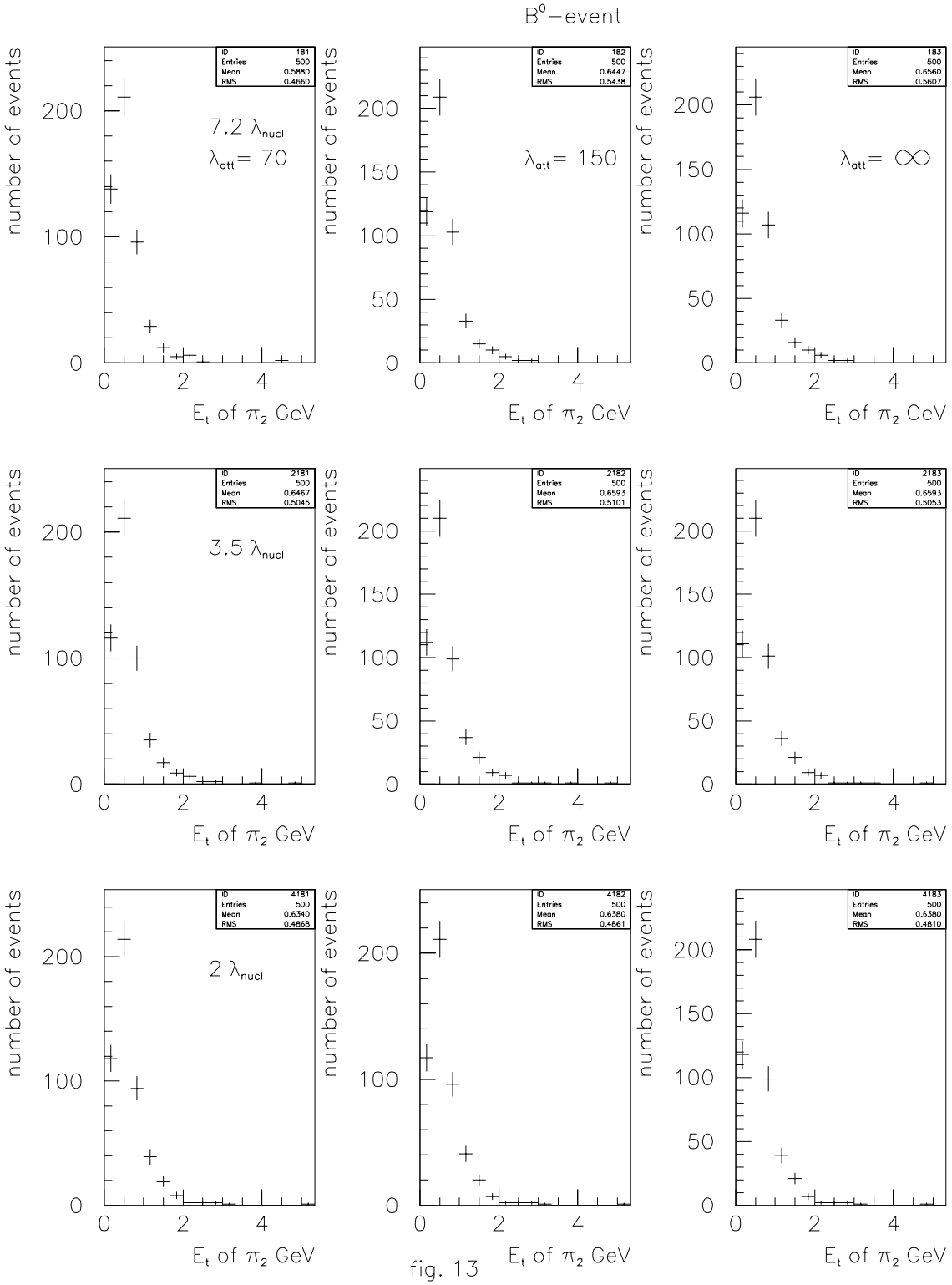

fig. 13

Distributions on the second pion transverse energy $E_t^{\pi_2}$ for different fiber attenuation length values λ_{att} and different values of hadronic calorimeter nuclear length for B_d^0 events.

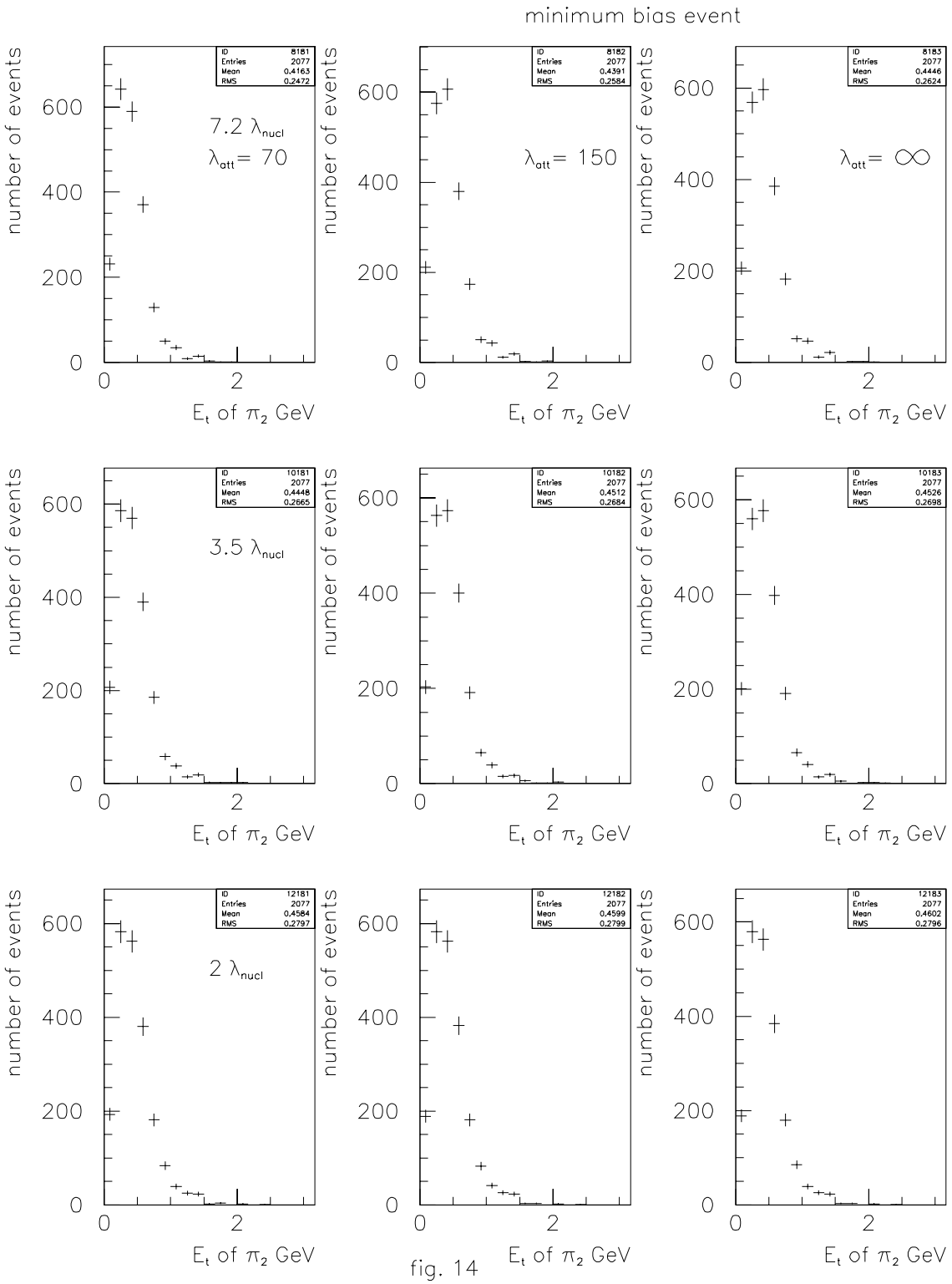

fig. 14

Distributions on the second pion transverse energy $E_t^{\pi_2}$ for different fiber attenuation length values λ_{att} and different values of hadronic calorimeter nuclear length for minimum bias events.

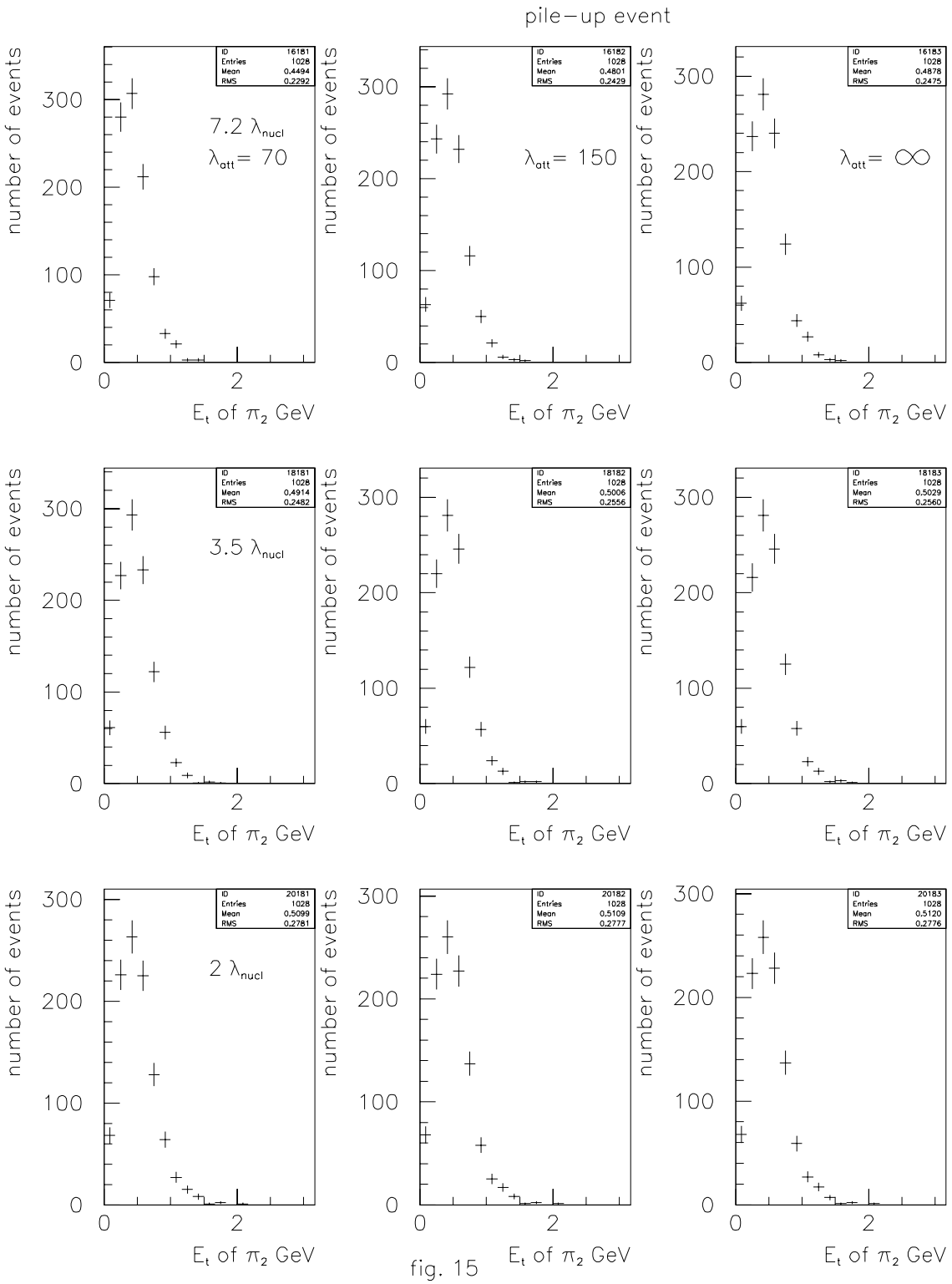

fig. 15

Distributions on the second pion transverse energy $E_t^{\pi_2}$ for different fiber attenuation length values λ_{att} and different values of hadronic calorimeter nuclear length for pile-up events.

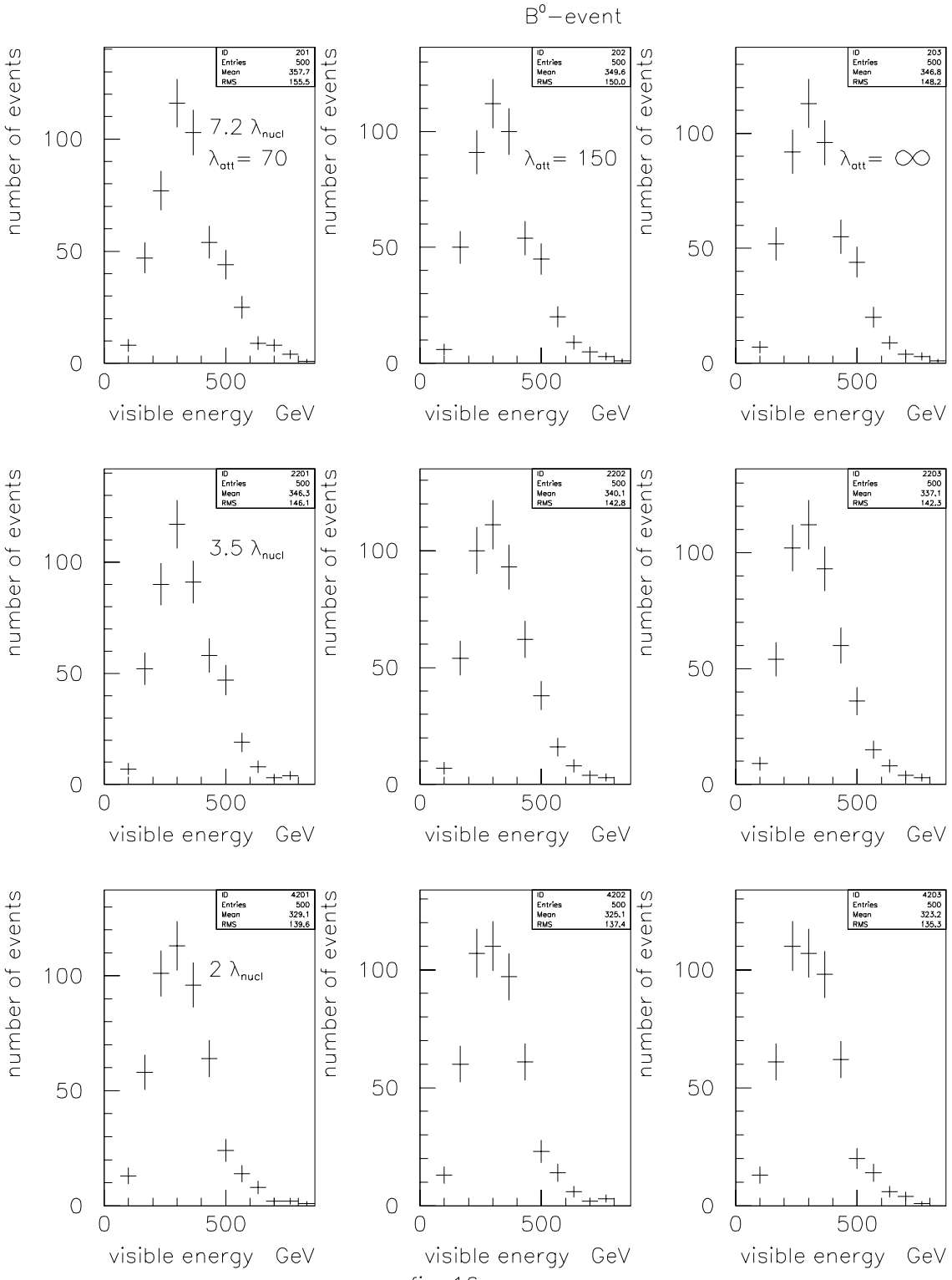

fig. 16

Distributions on the visible energy $E_{visible}$ deposited in the combined calorimeter for different fiber attenuation length values λ_{att} and different values of hadronic calorimeter nuclear length for B_d^0 events.

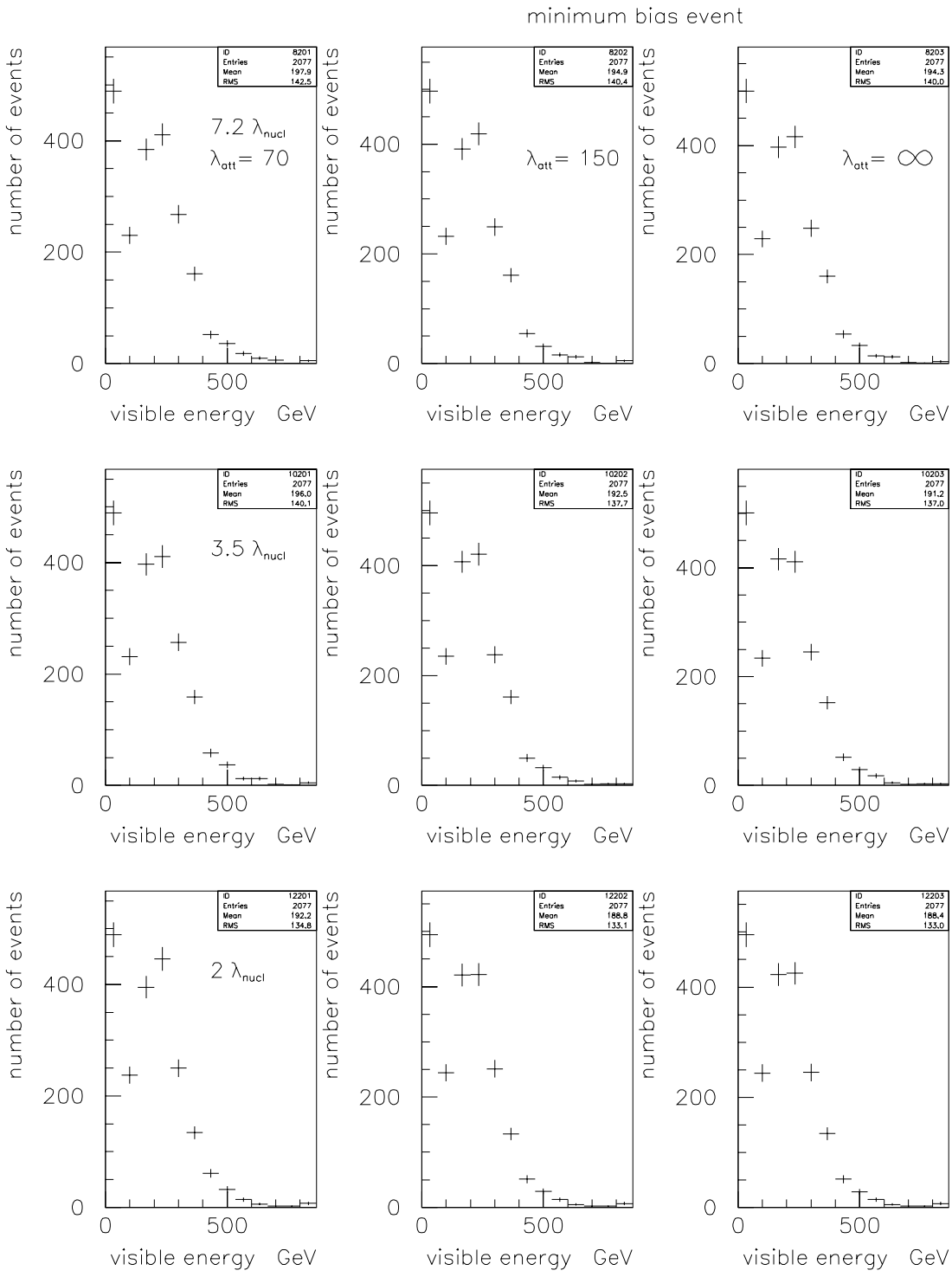

fig. 17

Distributions on the visible energy $E_{visible}$ deposited in the combined calorimeter for different fiber attenuation length values λ_{att} and different values of hadronic calorimeter nuclear length for minimum bias events.

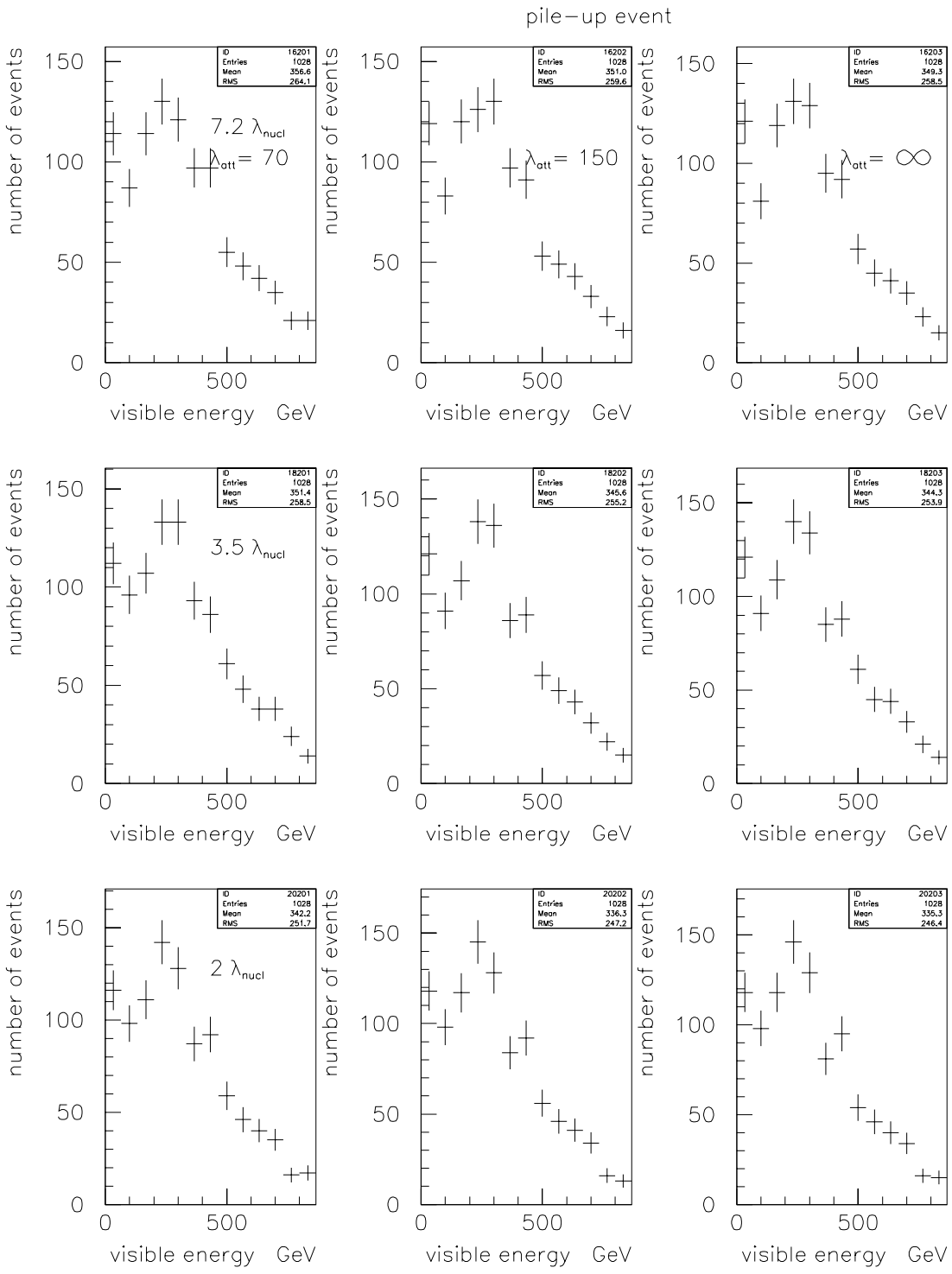

fig. 18

Distributions on the visible energy $E_{visible}$ deposited in the combined calorimeter for different fiber attenuation length values λ_{att} and different values of hadronic calorimeter nuclear length for pile-up events.

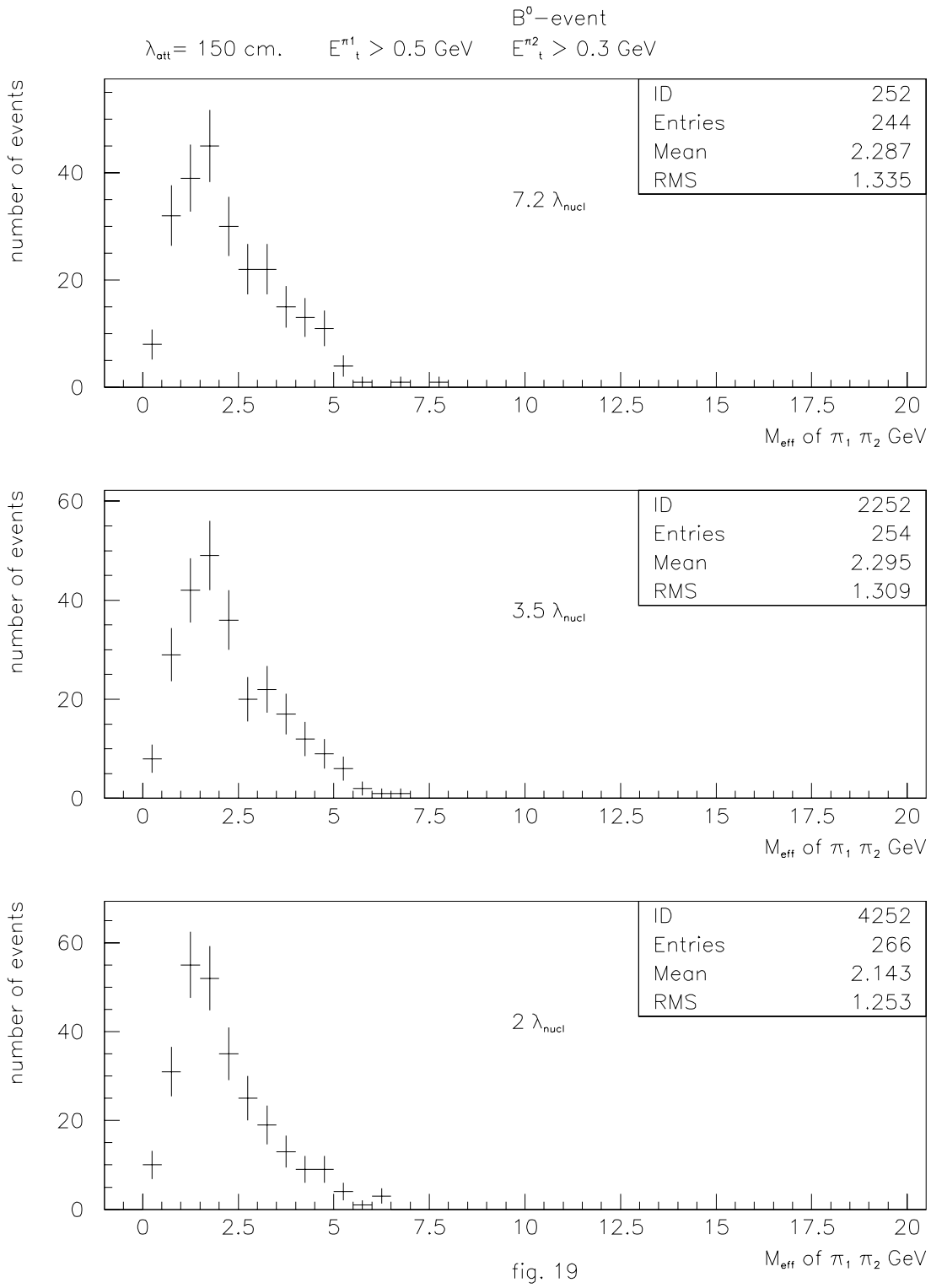

fig. 19

Distributions on the effective mass $M_{\pi_1\pi_2}$ of two selected π-mesons for fiber attenuation length $\lambda_{att} = 150$ cm, the transverse energy cuts $E_t^{\pi_1} > 0.5$ GeV, $E_t^{\pi_2} > 0.3$ GeV and different values of hadronic calorimeter nuclear length for B_d^0 events.

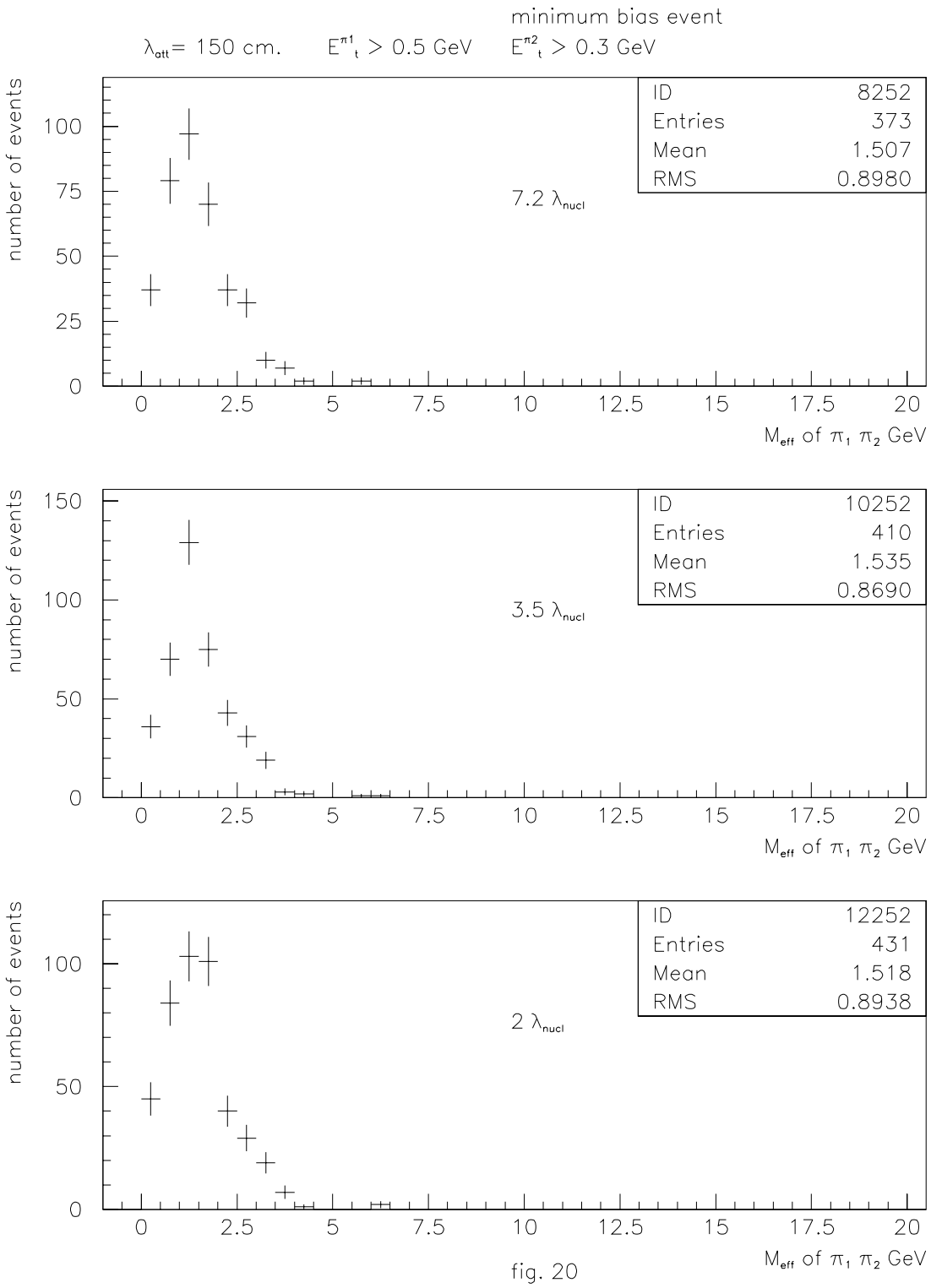

Distributions on the effective mass $M_{\pi_1\pi_2}$ of two selected π-mesons for fiber attenuation length $\lambda_{att} = 150$ cm, the transverse energy cuts $E_t^{\pi_1} > 0.5$ GeV, $E_t^{\pi_2} > 0.3$ GeV and different values of hadronic calorimeter nuclear length for minimum bias events.

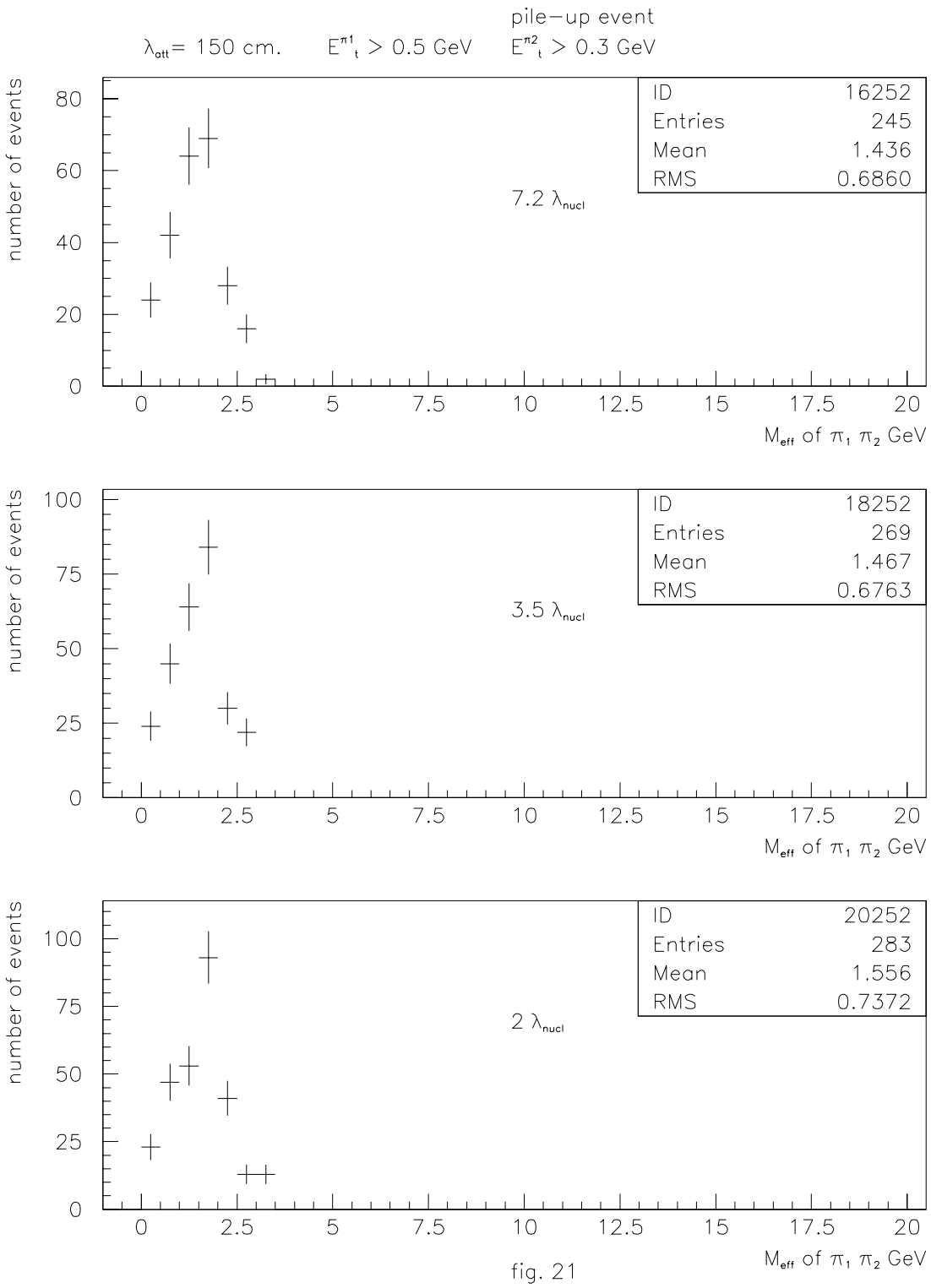

fig. 21

Distributions on the effective mass $M_{\pi_1\pi_2}$ of two selected π-mesons for fiber attenuation length $\lambda_{att} = 150$ cm, the transverse energy cuts $E_t^{\pi_1} > 0.5$ GeV, $E_t^{\pi_2} > 0.3$ GeV and different values of hadronic calorimeter nuclear length for pile-up events.

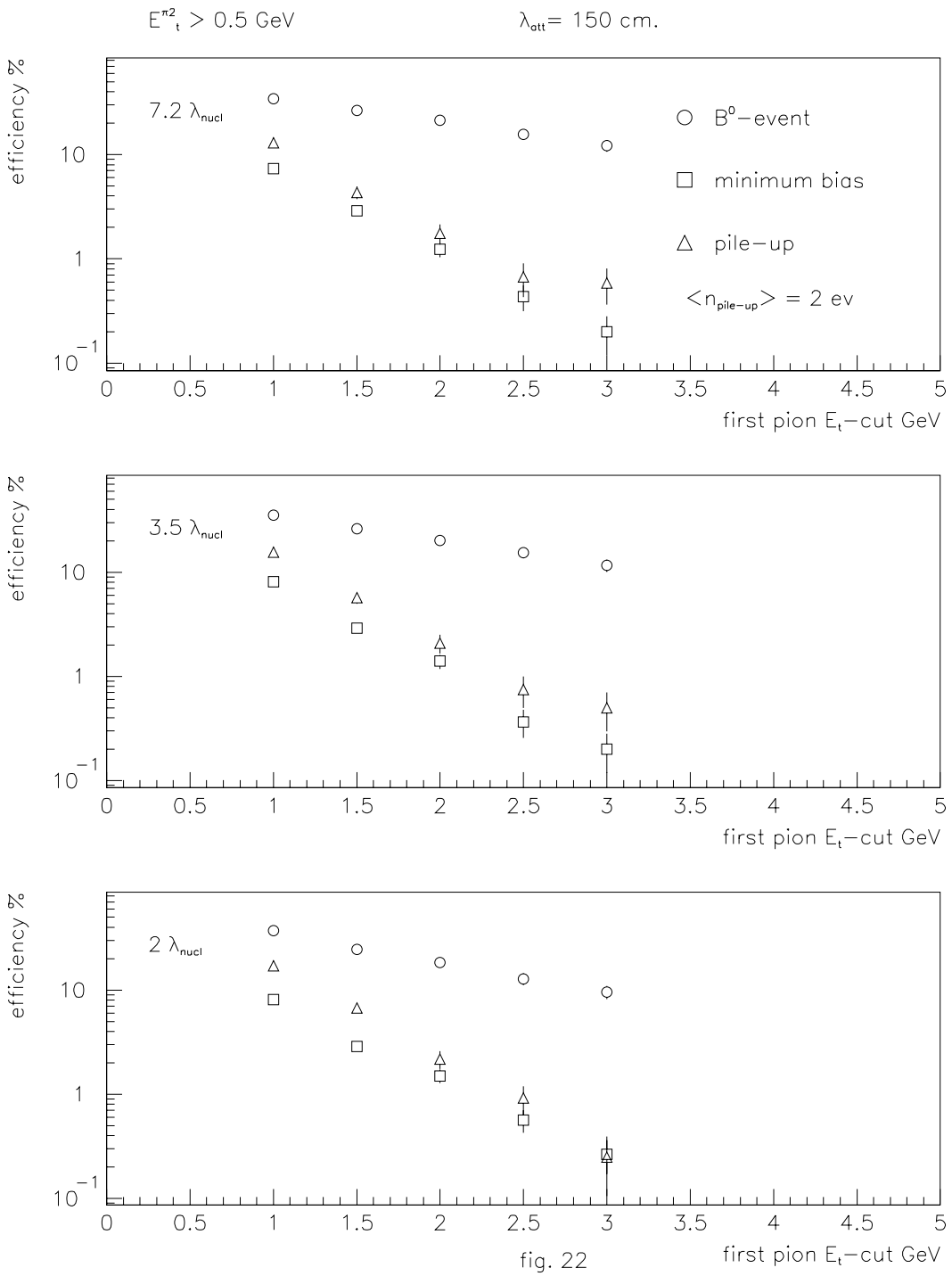

fig. 22

Dependence of the trigger efficiency ϵ on the first pion transverse energy $E_t^{\pi_1}$ for fiber attenuation length $\lambda_{att} = 150$ cm, the second pion transverse energy cut $E_t^{\pi_2} > 0.5$ GeV, the effective mass cut $M_{\pi_1\pi_2} > 0.5$ GeV , the visible energy cut $E_{visible} > 130$ GeV and different values of hadronic calorimeter nuclear length for B_d^0, minimum bias and pile-up events. The following cuts $E_{preclust} \leq 0.03$ GeV, $N_{preclust} \leq 4$, $R_{isol} \geq 6$ and $\frac{E_{clust}^{EMcal}}{E_{clust}^{Hcal}} \leq 60$ have been applied during precluster and cluster finding.

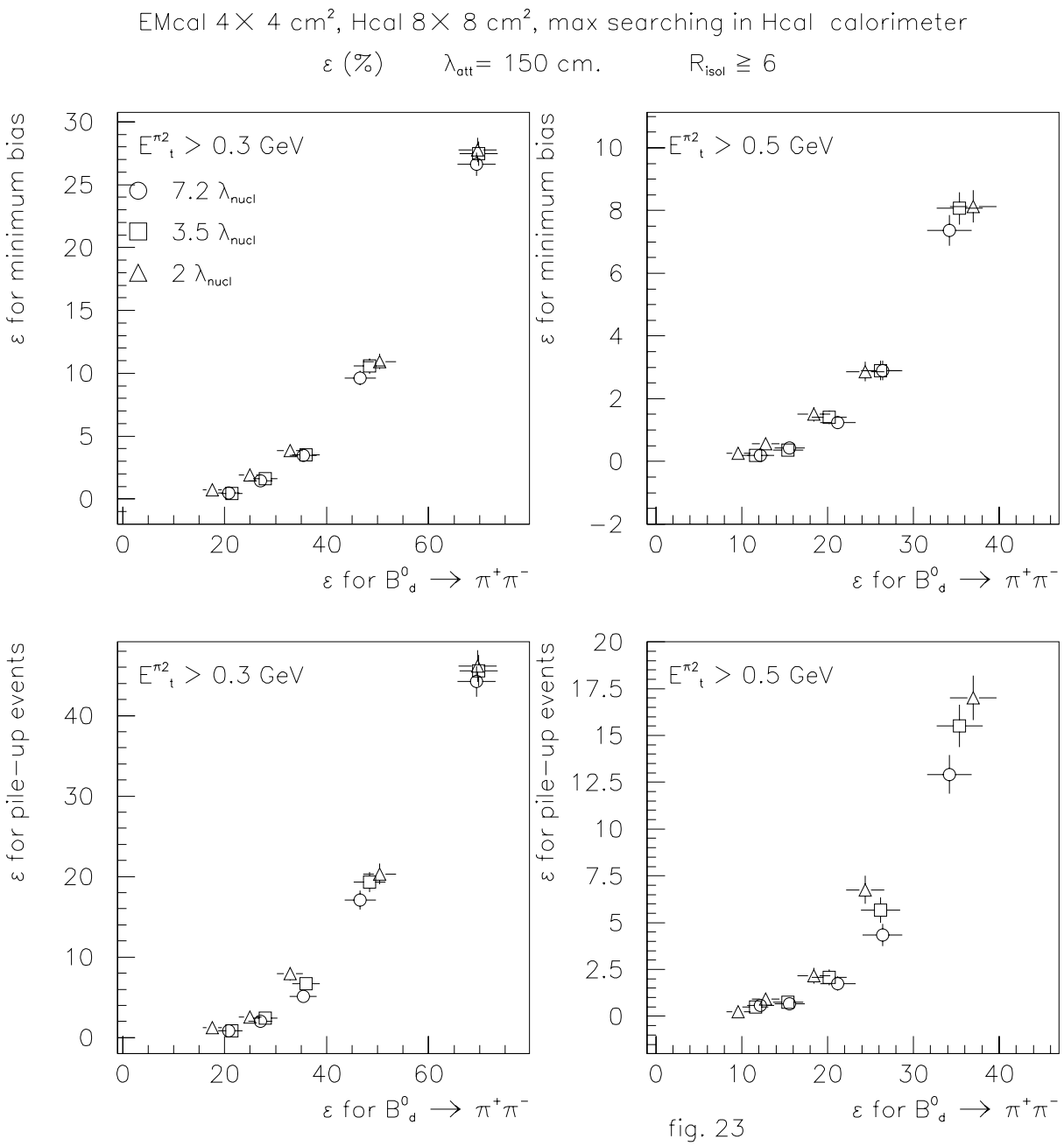

fig. 23

Dependence of the trigger efficiency ϵ for B_d^0-events on the minimum bias and pile-up efficiency for fiber attenuation length $\lambda_{att} = 150$ cm, the second pion transverse energy cut $E_t^{\pi_2} > 0.3$ and 0.5 GeV, the effective mass cut $M_{\pi_1\pi_2} > 0.5$ GeV , the visible energy cut $E_{visible} > 130$ GeV and hadronic calorimeter nuclear length $\lambda_{Hcal} = 2, 3.5, 7.2\ \lambda_{nucl}$. The following cuts $E_{preclust} \leq 0.03$ GeV, $N_{preclust} \leq 4$, $R_{isol} \geq 6$ and $\frac{E_{clust}^{EMcal}}{E_{clust}^{Hcal}} \leq 60$ have been applied during precluster and cluster finding.

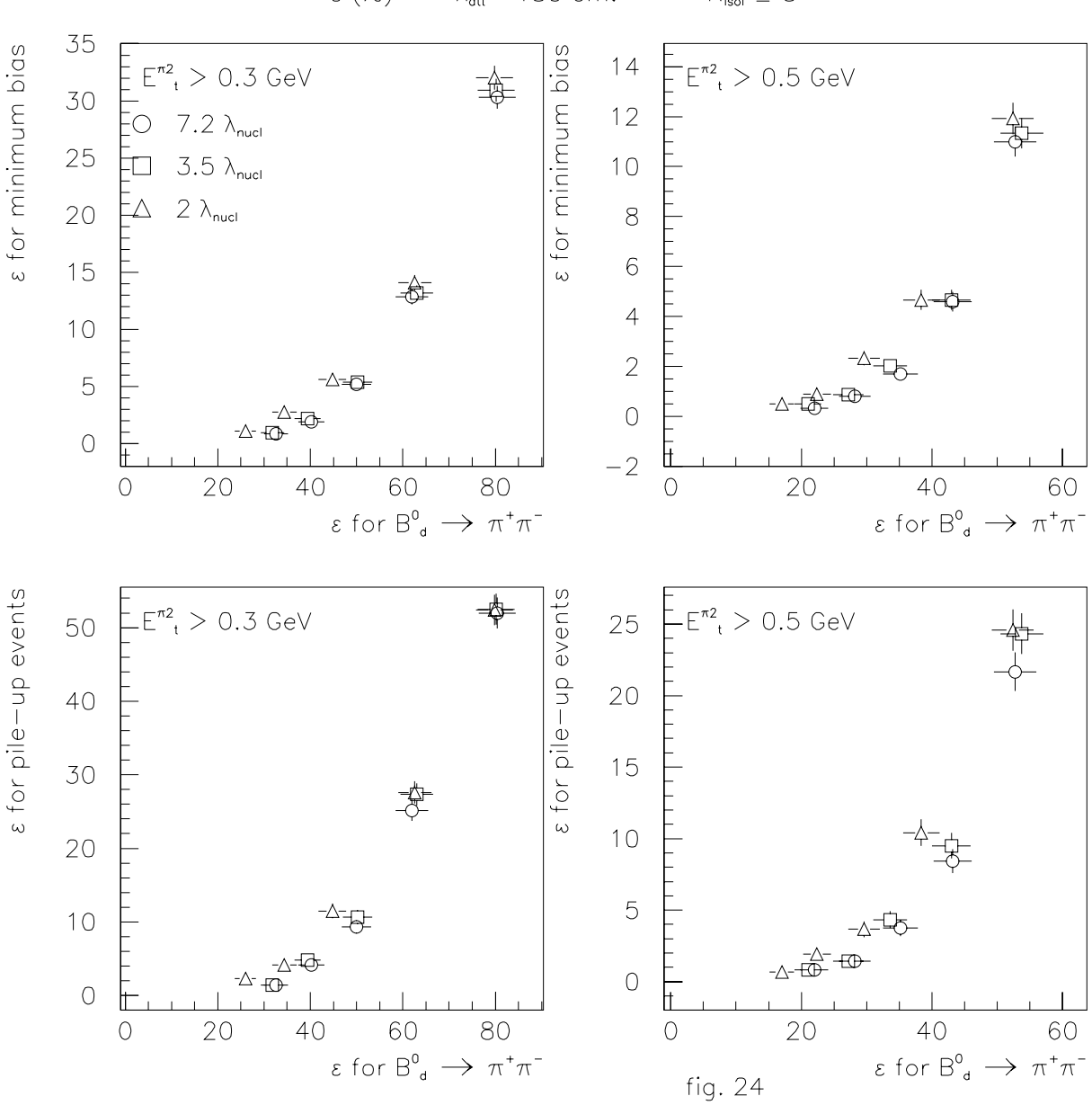

fig. 24

Dependence of the trigger efficiency ϵ for B_d^0-events on the minimum bias and pile-up efficiency for fiber attenuation length $\lambda_{att} = 150$ cm, the second pion transverse energy cut $E_t^{\pi_2} > 0.3$ and 0.5 GeV, the effective mass cut $M_{\pi_1\pi_2} > 0.5$ GeV , the visible energy cut $E_{visible} > 130$ GeV and hadronic calorimeter nuclear length $\lambda_{Hcal} = 2,\ 3.5,\ 7.2\ \lambda_{nucl}$. The following cuts $E_{preclust} \leq 0.03$ GeV, $N_{preclust} \leq 4$, $R_{isol} \geq 3$ and $\frac{E_{clust}^{EMcal}}{E_{clust}^{Hcal}} \leq 60$ have been applied during precluster and cluster finding.

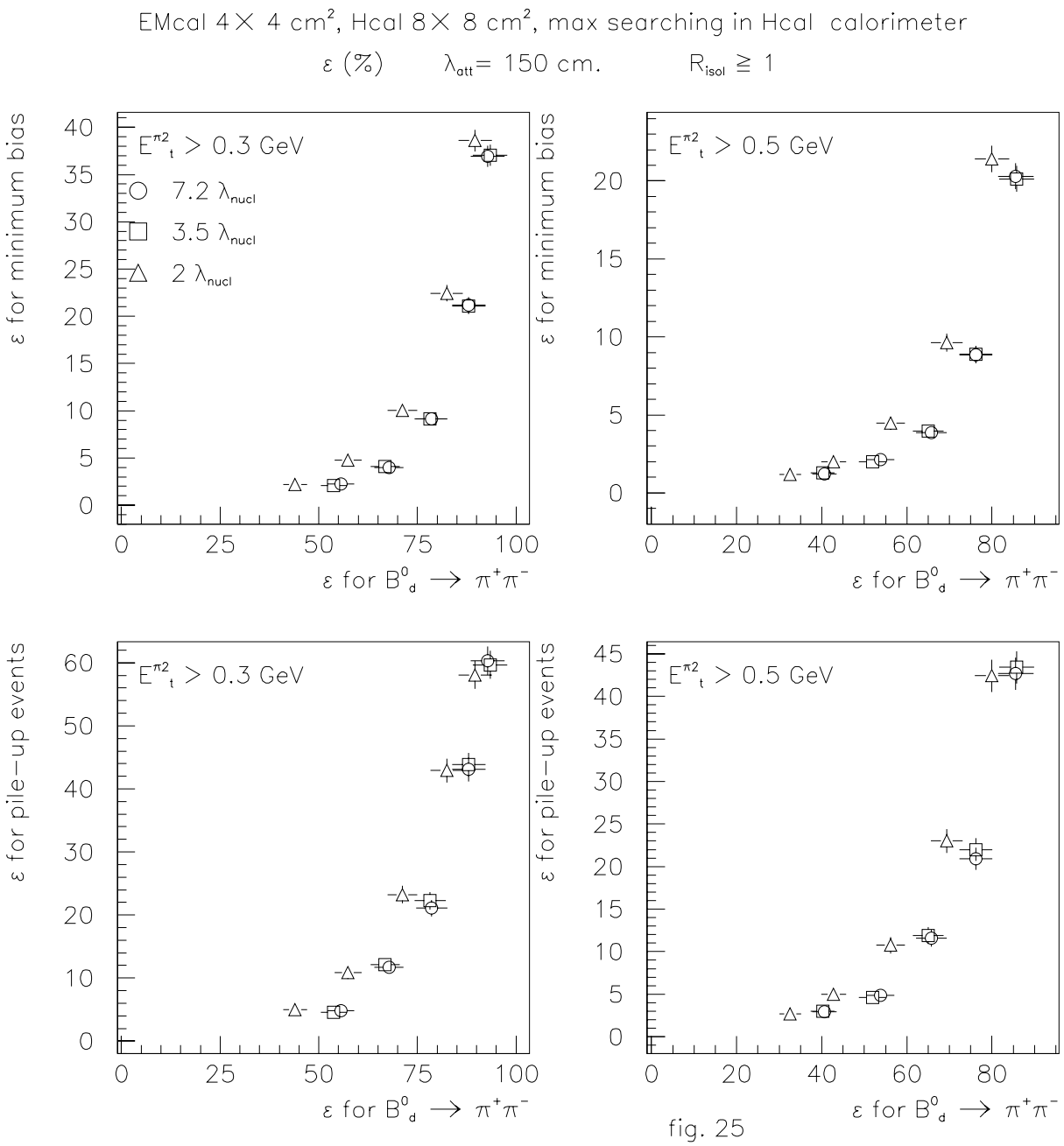

fig. 25

Dependence of the trigger efficiency ϵ for B_d^0-events on the minimum bias and pile-up efficiency for fiber attenuation length $\lambda_{att} = 150$ cm, the second pion transverse energy cut $E_t^{\pi_2} > 0.3$ and 0.5 GeV, the effective mass cut $M_{\pi_1\pi_2} > 0.5$ GeV , the visible energy cut $E_{visible} > 130$ GeV and hadronic calorimeter nuclear length $\lambda_{Hcal} = 2,\ 3.5,\ 7.2\ \lambda_{nucl}$. The following cuts $E_{preclust} \leq 0.03$ GeV, $N_{preclust} \leq 4$, $R_{isol} \geq 1$ and $\frac{E_{clust}^{EMcal}}{E_{clust}^{Hcal}} \leq 60$ have been applied during precluster and cluster finding.

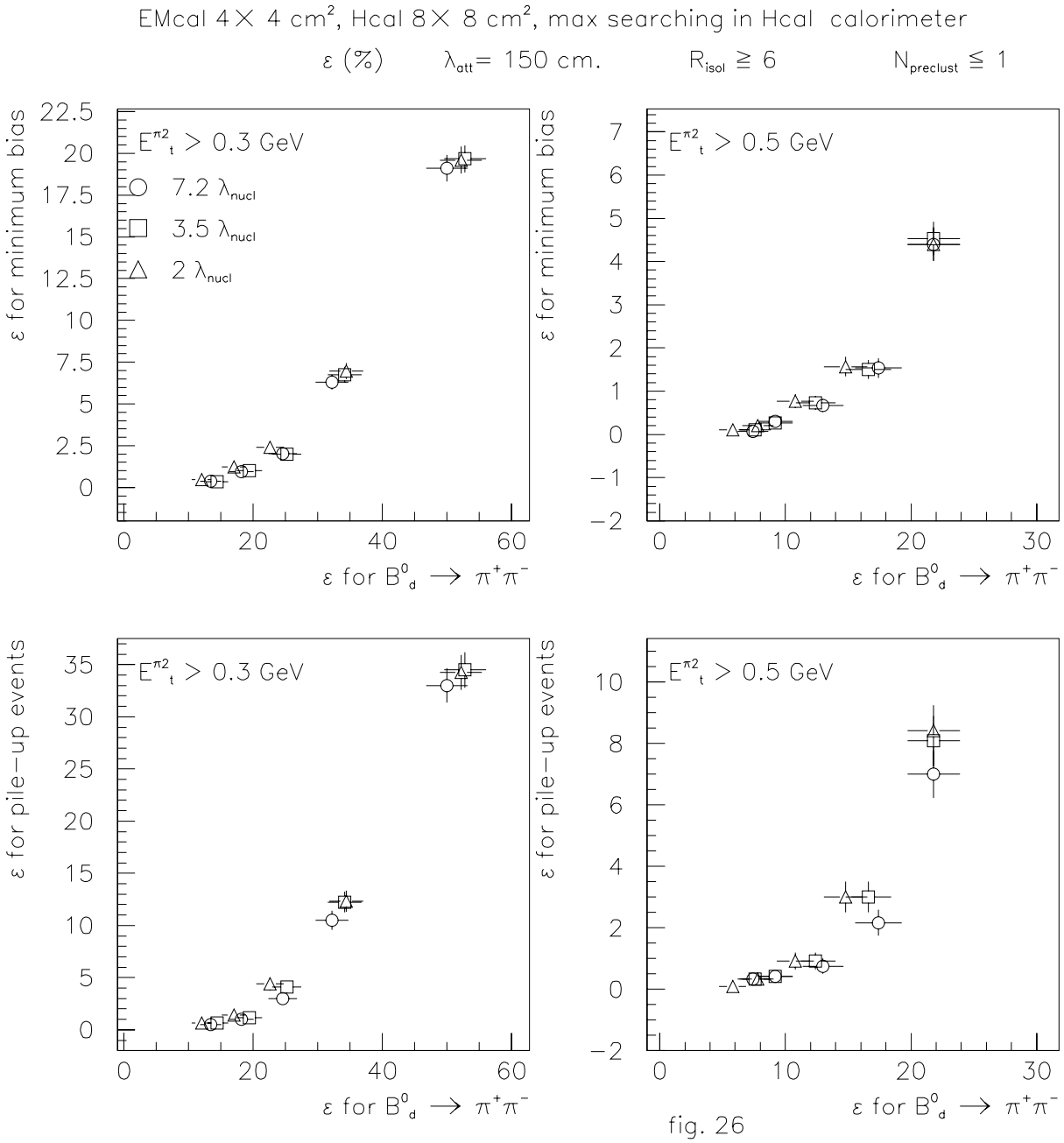

fig. 26

Dependence of the trigger efficiency ϵ for B_d^0-events on the minimum bias and pile-up efficiency for fiber attenuation length $\lambda_{att} = 150$ cm, the second pion transverse energy cut $E_t^{\pi_2} > 0.3$ and 0.5 GeV, the effective mass cut $M_{\pi_1\pi_2} > 0.5$ GeV, the visible energy cut $E_{visible}$ >130 GeV and hadronic calorimeter nuclear length $\lambda_{Hcal} = 2, 3.5, 7.2\ \lambda_{nucl}$. The following cuts $E_{preclust} \leq 0.03$ GeV, $N_{preclust} \leq 1$, $R_{isol} \geq 6$ and $\frac{E_{clust}^{EMcal}}{E_{clust}^{Hcal}} \leq 60$ have been applied during precluster and cluster finding.

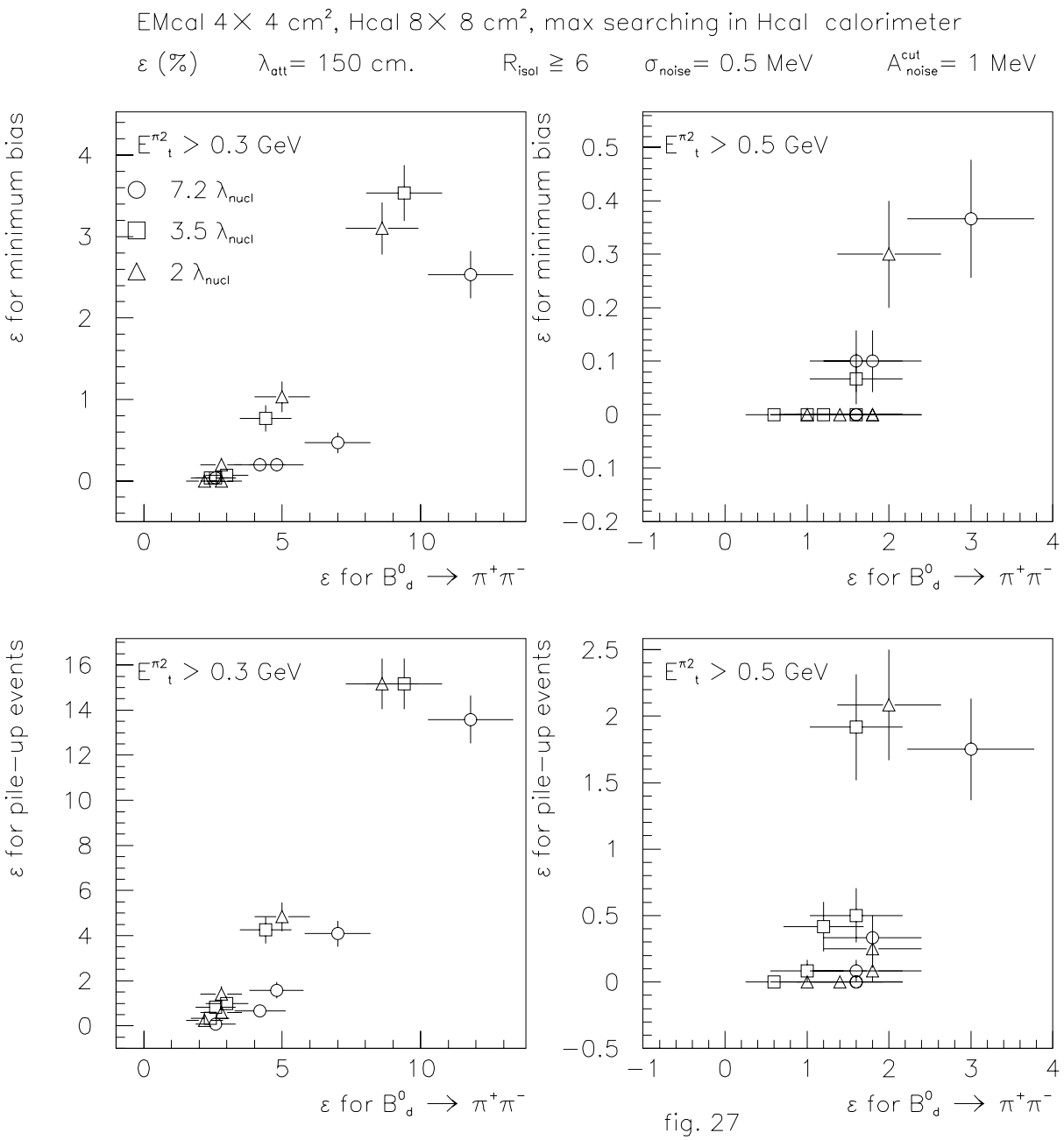

fig. 27

Dependence of the trigger efficiency ϵ for B_d^0-events on the minimum bias and pile-up efficiency for fiber attenuation length $\lambda_{att} = 150$ cm, the second pion transverse energy cut $E_t^{\pi_2} > 0.3$ and 0.5 GeV, the effective mass cut $M_{\pi_1\pi_2} > 0.5$ GeV, the visible energy cut $E_{visible}$ >130 GeV and hadronic calorimeter nuclear length $\lambda_{Hcal} = 2, 3.5, 7.2\ \lambda_{nucl}$. The following cuts $E_{preclust} \leq 0.03$ GeV, $N_{preclust} \leq 4$, $R_{isol} \geq 6$ and $\frac{E_{clust}^{EMcal}}{E_{clust}^{Hcal}} \leq 60$ have been applied during precluster and cluster finding. The width of Gaussian noise amplitude distribution is $\sigma_{noise} = 0.5$ MeV. The cut on the noise amplitude is $A_{cut}^{noise} = 1$ MeV.

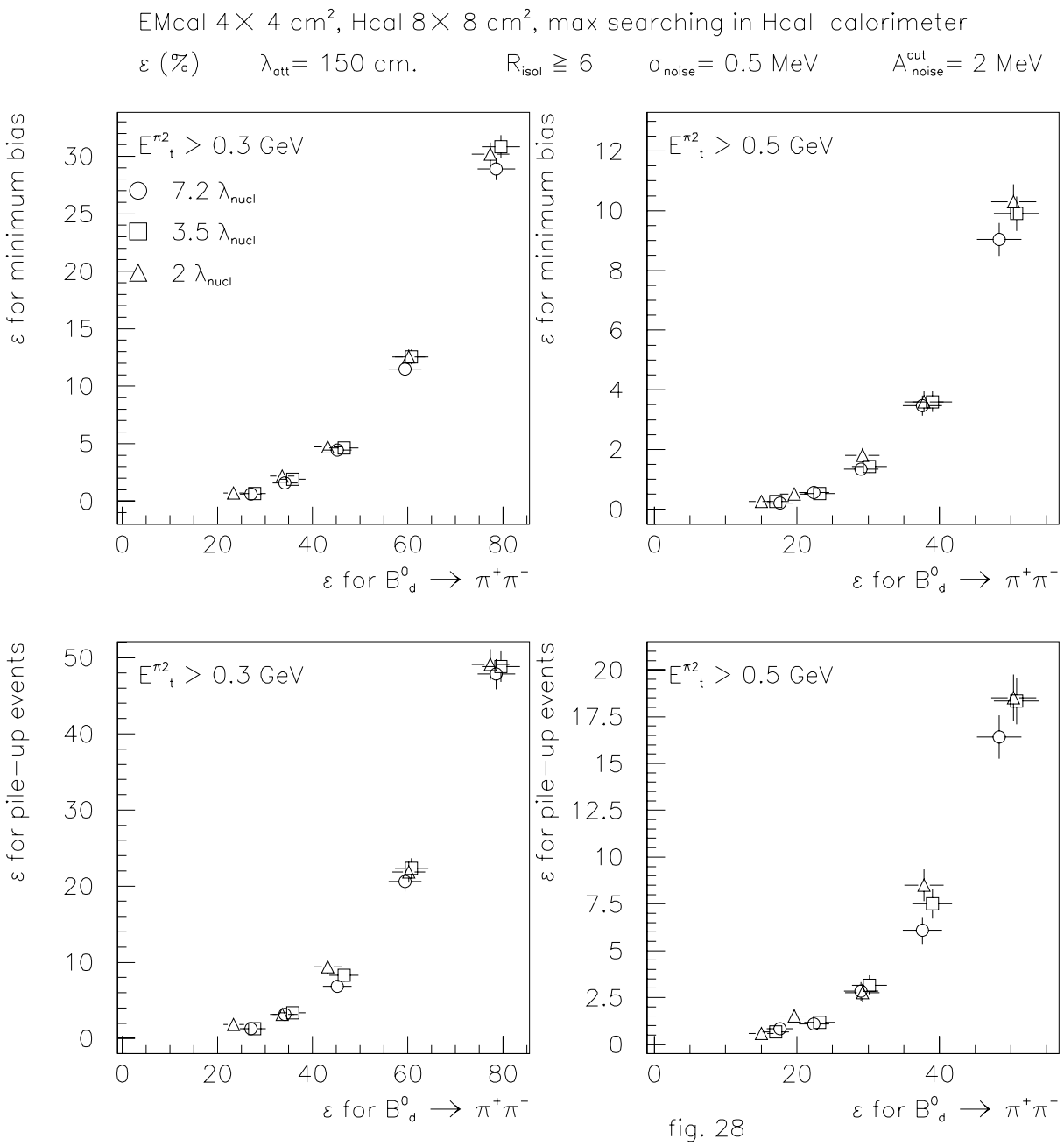

fig. 28

Dependence of the trigger efficiency ϵ for B_d^0-events on the minimum bias and pile-up efficiency for fiber attenuation length λ_{att} = 150 cm, the second pion transverse energy cut $E_t^{\pi_2} > 0.3$ and 0.5 GeV, the effective mass cut $M_{\pi_1\pi_2} > 0.5$ GeV, the visible energy cut $E_{visible}$ >130 GeV and hadronic calorimeter nuclear length $\lambda_{Hcal} = 2, 3.5, 7.2\ \lambda_{nucl}$. The following cuts $E_{preclust} \leq 0.03$ GeV, $N_{preclust} \leq 4$, $R_{isol} \geq 6$ and $\frac{E_{clust}^{EMcal}}{E_{clust}^{Hcal}} \leq 60$ have been applied during precluster and cluster finding. The width of Gaussian noise amplitude distribution is σ_{noise} =0.5 MeV. The cut on the noise amplitude is A_{cut}^{noise} =2 MeV.

References

[1] L. Wolfenstein, Phys. Rev. D31 (1985) 2381.

[2] LHC-B, LOI.

[3] GEANT 3.21, CERN Program Library Long Writeup W5013.

[4] T.Sjostrand PYTHIA 5.7, CERN-TH.7112/93 CERN Program Library Long Writeup W5035.

Received December 30, 1999

В. Бумажнов и др.
Эффективность калориметрического триггера в эксперименте LHC-B для процесса $pp \to (B_d^0 \to \pi^+\pi^-) + X$ at $\sqrt{S}$ =14 TeV.

Оригинал-макет подготовлен с помощью системы LaTeX.
Редактор Е.Н.Горина. Технический редактор Н.В.Орлова.

Подписано к печати 31.12.99. Формат 60 × 84/8. Офсетная печать.
Печ.л. 6.25. Уч.-изд.л. 5. Тираж 160. Заказ 24. Индекс 3649.
ЛР №020498 17.04.97.

ГНЦ РФ Институт физики высоких энергий
142284, Протвино Московской обл.

Индекс 3649

П Р Е П Р И Н Т 99–63, И Ф В Э, 1999